# Multicomponent flow on curved surfaces: A vielbein lattice Boltzmann approach

Victor E. Ambruş ●,[1,*] Sergiu Busuioc ●,[1] Alexander J. Wagner,[2] Fabien Paillusson,[3] and Halim Kusumaatmaja[4,†]

[1]*Department of Physics, West University of Timişoara, 300223 Timişoara, Romania*
[2]*Department of Physics, North Dakota State University, Fargo, North Dakota 58108, USA*
[3]*School of Mathematics and Physics, University of Lincoln, Lincoln LN6 7TS, United Kingdom*
[4]*Department of Physics, Durham University, Durham, DH1 3LE, United Kingdom*

We develop and implement a finite difference lattice Boltzmann scheme to study multicomponent flows on curved surfaces, coupling the continuity and Navier-Stokes equations with the Cahn-Hilliard equation to track the evolution of the binary fluid interfaces. The standard lattice Boltzmann method relies on regular Cartesian grids, which makes it generally unsuitable to study flow problems on curved surfaces. To alleviate this limitation, we use a vielbein formalism to write the Boltzmann equation on an arbitrary geometry, and solve the evolution of the fluid distribution functions using a finite difference method. Focusing on the torus geometry as an example of a curved surface, we demonstrate drift motions of fluid droplets and stripes embedded on the surface of the torus. Interestingly, they migrate in opposite directions: fluid droplets to the outer side while fluid stripes to the inner side of the torus. For the latter we demonstrate that the global minimum configuration is unique for small stripe widths, but it becomes bistable for large stripe widths. Our simulations are also in agreement with analytical predictions for the Laplace pressure of the fluid stripes, and their damped oscillatory motion as they approach equilibrium configurations, capturing the corresponding decay timescale and oscillation frequency. Finally, we simulate the coarsening dynamics of phase separating binary fluids in the hydrodynamics and diffusive regimes for tori of various shapes, and compare the results against those for a flat two-dimensional surface. Our finite difference lattice Boltzmann scheme can be extended to other surfaces and coupled to other dynamical equations, opening up a vast range of applications involving complex flows on curved geometries.

## I. INTRODUCTION

Hydrodynamics on curved manifolds is relevant for a wide range of physical phenomena. Examples range from the motion of electrons in graphene at the microscale [1], through thin liquid films [2,3], confined active matter [4–6] and biomembranes [7,8] at the mesoscale, to relativistic flows in astrophysics [9] and at the cosmological scale [10]. However, despite its importance, the study of flows on curved space has received much less attention when compared to corresponding investigations on two- and three-dimensional flat space. Suitable numerical approaches to study these problems are also still limited, especially when the flow phenomena of interest involve several fluid components.

Here, our focus is on multicomponent flow on curved two-dimensional surfaces. An important motivation to study such problem arises from biological membranes and their synthetic counterparts. Experimentally, it has been observed that self-assembled lipid and polymer membranes can adopt an astonishing range of shapes and morphologies [11], from single bilayers to stacks and convoluted periodic structures. Moreover, these membranes are usually comprised of several species, which can mix or demix depending on the thermodynamic conditions under which they are prepared [12–14]. The

interplay between curvature and composition is a ubiquitous structural feature for biomembranes, and they are key to biological functions and synthetic membrane-based applications [15–17].

There is much interest to understand this interplay between membrane curvature and composition. However, to date continuum modeling of membranes with several lipid components have largely focused on their equilibrium configurations [18–21]. Several dynamic studies of phase separation on curved surfaces have been carried out in the literature. However, apart from a few exceptions [22], they usually involve diffusive dynamics and ignore the importance of hydrodynamics [23–25]. The aim of this paper is to develop a flexible finite difference lattice Boltzmann framework to simulate multicomponent flow on arbitrary curved surfaces. For simplicity, here we will assume the two-dimensional flow is Newtonian. For lipid membranes, this assumption is supported by both molecular dynamics simulations and experimental observations [26–29].

Our approach is based on the lattice Boltzmann method (LBM) [30,31], which has recently become increasingly popular to study multicomponent flow phenomena, with good agreement against experiments and other simulation methods, including for drop dynamics, liquid phase separation, microfluidics, and porous media [32–35]. Within the lattice Boltzmann literature, there are several models for multicomponent flow, including the so-called free energy [36], pseudopotential [37], and color [38] models. In this work, we have

*victor.ambrus@e-uvt.ro
†halim.kusumaatmaja@durham.ac.uk

chosen to employ the free energy model, though our framework can be adapted to account for the pseudopotential and color models. Our approach can also be extended to account for more fluid components [39–43], as well as coupled to other dynamical equations, including those for liquid crystals [44,45] and viscoelastic fluids [46,47].

Standard lattice Boltzmann method is based on regular Cartesian grids. In recent years, several groups proposed its extension to the case of curvilinear coordinates. Of these extensions, we mention three groups of approaches. In the first, exact streaming is preserved [48–51] and the equilibrium distribution exhibits metric-dependent terms. Furthermore, a source term is added to enable the recovery of the covariant Navier-Stokes equations through the Chapman-Enskog expansion. This approach transfers the metric dependence from the streaming part to the forcing and collision parts. In the second approach, the transformation to curvilinear coordinates is performed in the streaming operator [52–55]. The velocity space degrees of freedom are still the Cartesian ones. In this approach, the equilibrium distribution is unmodified and no source terms are required. However, exact streaming is lost because the advection velocities become coordinate dependent. Finally, the third approach employs a transformation of the velocity space degrees of freedom, allowing these to retain the symmetries of the curvilinear coordinate grid. This approach has been commonly used in the discrete velocity method (DVM) community [56,57]. Recently, this approach was formulated in a general way by use of differential geometry and vielbein fields [58], in the spirit of previous work on kinetic theory in general relativity [59]. In this approach, the advection velocities become coordinate independent, allowing the dimensionality of problems with a given symmetry to be reduced. In this paper, we employ the latter approach, due to its versatility in treating more complex geometries. Thus, our implementation relies on finite difference techniques for the implementation of the time stepping and advection parts of the lattice Boltzmann algorithm.

The capabilities of our method are demonstrated using several problems. First, we study drift motion of fluid droplets and stripes when placed on the surface of a torus. This drift is due to nonuniform curvature and, as such, is not present on flat space, or for surfaces with uniform curvature (e.g., a sphere). For the stripes, analytical results are available for their equilibrium configuration, Laplace pressure, and relaxation dynamics [60], thus providing an excellent platform to systematically examine the accuracy of our method. We demonstrate that these predictions are accurately captured in our simulations. Second, we simulate binary phase separation on the surface of a torus for equal and unequal compositions, both in diffusive and hydrodynamic regimes. We compare and contrast the results for tori of various shapes against those for flat two-dimensional surface [61–63].

## II. COMPUTATIONAL MODEL AND METHOD

In this section we develop a framework that allows simulations of multicomponent flow on arbitrary curved surfaces. Our vielbein finite difference lattice Boltzmann approach has three key features. First, similar to standard lattice Boltzmann method, we exploit the Boltzmann equation to solve the

continuum equations of motion, and we use a discrete and finite set of fluid distribution functions. Second, unlike standard lattice Boltzmann method, the discrete velocity sets do not coincide with the neighboring lattice points. Thus, rather than solving the Boltzmann equation using a sequence of collision and propagation steps, we take advantage of a finite difference method. Third, to describe the curved surface, we employ a vielbein field, which decouples the velocity space from the coordinate space [58,59]. This simplifies the formulation and computation of the governing Boltzmann equation.

### A. Brief introduction to vielbein fields

Let us begin by considering a two-dimensional curved surface embedded in three dimensions. Vector fields, such as the velocity field $\boldsymbol{u}(\boldsymbol{x})$, on the two-dimensional surface can be expressed in the curvilinear coordinate system using

$$\boldsymbol{u}(\boldsymbol{x}) = u^a(q^b)\boldsymbol{\partial}_a, \tag{2.1}$$

where $u^a(q^b)$ represent the components of the velocity field on a manifold parametrized using the coordinates $q^b$ ($1 \leqslant a, b \leqslant 2$ for two-dimensional manifolds). Furthermore, the squared norm of the velocity field $\boldsymbol{u}$ can be computed as

$$\boldsymbol{u}^2 = g_{ab}u^a u^b, \tag{2.2}$$

where $g_{ab}$ is called the metric tensor. This description of vector fields in curvilinear coordinates can become inconvenient for practical computations. This is because the elements of the metric tensor $g_{ab}$ may become singular at various points due to the choice of surface parametrization. In such instances, the contravariant components $u^a$ of the velocity must diverge in order for the squared norm $\boldsymbol{u}^2$ to remain finite.

The difficulty described above can be alleviated by introducing, as an interface between the coordinate space and the space of vectors, the vielbein vector fields (frame) $\boldsymbol{e}_{\hat{a}} = e^a_{\hat{a}}\boldsymbol{\partial}_a$. Dual to the vielbein vector fields are the vielbein one-forms (coframe) $\boldsymbol{\omega}^{\hat{a}} = \omega^{\hat{a}}_a \boldsymbol{dq}^a$. We reserve the hatted indices to denote the vielbein framework. The vielbein frame and coframe have to satisfy the following relations:

$$\omega^{\hat{a}}_a e^a_{\hat{b}} = \delta^{\hat{a}}_{\hat{b}}, \quad \omega^{\hat{a}}_a e^b_{\hat{a}} = \delta^b_a, \quad g_{ab}e^a_{\hat{a}}e^b_{\hat{b}} = \delta_{\hat{a}\hat{b}}. \tag{2.3}$$

With the above vielbein frame and coframe, the vector field $\boldsymbol{u}$ can be written as

$$\boldsymbol{u} = u^{\hat{a}}\boldsymbol{e}_{\hat{a}}, \tag{2.4}$$

where the vector field components are

$$u^{\hat{a}} = \omega^{\hat{a}}_a u^a, \quad u^a = e^a_{\hat{a}}u^{\hat{a}}, \tag{2.5}$$

and the squared norm

$$\boldsymbol{u}^2 = \delta_{\hat{a}\hat{b}}u^{\hat{a}}u^{\hat{b}}. \tag{2.6}$$

In the vielbein framework, the information on the metric tensor is effectively absorbed in the components of the vector field, which makes the formulation and derivation of the lattice Boltzmann approach significantly less cumbersome.

In the lattice Boltzmann implementation used in this paper, we need to introduce two more geometrical objects. First, the Cartan coefficients $c_{\hat{a}\hat{b}}{}^{\hat{c}}$ are defined as

$$c_{\hat{a}\hat{b}}{}^{\hat{c}} = ([\boldsymbol{e}_{\hat{a}}, \boldsymbol{e}_{\hat{b}}])^a \omega^{\hat{c}}_a, \tag{2.7}$$

with the commutator $([\boldsymbol{e}_{\hat{a}}, \boldsymbol{e}_{\hat{b}}])^a = e_{\hat{a}}^b \partial_b e_{\hat{b}}^a - e_{\hat{b}}^b \partial_b e_{\hat{a}}^a$. Second, $\Gamma^{\hat{d}}_{\ \hat{b}\hat{c}}$ and $\Gamma_{\hat{a}\hat{b}\hat{c}}$ represent the connection coefficients, which are defined as

$$\Gamma^{\hat{d}}_{\ \hat{b}\hat{c}} = \delta^{\hat{d}\hat{a}} \Gamma_{\hat{a}\hat{b}\hat{c}}, \quad \Gamma_{\hat{a}\hat{b}\hat{c}} = \tfrac{1}{2}(c_{\hat{a}\hat{b}\hat{c}} + c_{\hat{a}\hat{c}\hat{b}} - c_{\hat{b}\hat{c}\hat{a}}). \quad (2.8)$$

In Appendix A, we detail the application of the vielbein formalism for a torus. It is worth noting that our approach is general and other curved geometries can be handled in a similar way.

### B. Binary fluid model and equations of motion

We consider a binary mixture of fluids $A$ and $B$, characterized by an order parameter $\phi$, such that $\phi = 1$ corresponds to a bulk fluid $A$ and $\phi = -1$ to a bulk fluid $B$. A simple free energy model that allows the coexistence of these two bulk fluids is given by the following Landau free energy [30,64]:

$$\Psi = \int_V \left[ \frac{A}{4}(1 - \phi^2)^2 + \frac{\kappa}{2}(\nabla\phi)^2 \right] dV, \quad (2.9)$$

where $A$ and $\kappa$ are free parameters, which are related to the interface width $\xi_0$ and surface tension $\gamma$ through

$$\xi_0 = \sqrt{\frac{\kappa}{A}}, \quad \gamma = \sqrt{\frac{8\kappa A}{9}}. \quad (2.10)$$

The chemical potential can be derived by taking the functional derivative of the free energy with respect to the order parameter, giving

$$\mu(\boldsymbol{x}) = \frac{\delta\Psi}{\delta\phi(\boldsymbol{x})} = -A\phi(1 - \phi^2) - \kappa\Delta\phi. \quad (2.11)$$

The evolution of the order parameter $\phi$ is specified by the Cahn-Hilliard equation. In covariant form it is given by

$$\partial_t \phi + \nabla_{\hat{a}}(u^{\hat{a}}\phi) = \nabla_{\hat{a}}(M\nabla^{\hat{a}}\mu), \quad (2.12)$$

where the hatted indices are taken with respect to the orthonormal vielbein basis. Equivalently, indices with respect to coordinate basis can be used, e.g., $\nabla_{\hat{a}}(u^{\hat{a}}\phi) = \nabla_a(u^a\phi)$. In the above, $M$ is the mobility parameter, $\mu$ is the chemical potential, and the fluid velocity $\boldsymbol{u}$ is a solution of the continuity and Navier-Stokes equations

$$\partial_t n + \nabla_{\hat{a}}(u^{\hat{a}}n) = 0, \quad \rho\frac{Du^{\hat{a}}}{Dt} = -\nabla_{\hat{b}}T^{\hat{a}\hat{b}} + nF^{\hat{a}}, \quad (2.13)$$

where $D/Dt = \partial_t + u^{\hat{b}}\nabla_{\hat{b}}$ is the material (convective) derivative, $m$ is the particle mass, $n$ is the number density, and $\rho = mn$. The stress tensor $T^{\hat{a}\hat{b}} = p_i\delta^{\hat{a}\hat{b}} + \sigma^{\hat{a}\hat{b}}$ is that of a viscous ideal gas, where $p_i = nk_B T$ is the pressure of the ideal gas and $\sigma^{\hat{a}\hat{b}}$ is the viscous stress for the Newtonian fluid [65]:

$$\sigma^{\hat{a}\hat{b}} = -\eta(\nabla^{\hat{a}}u^{\hat{b}} + \nabla^{\hat{b}}u^{\hat{a}} - \delta^{\hat{a}\hat{b}}\nabla_{\hat{c}}u^{\hat{c}}) - \eta_v\delta^{\hat{a}\hat{b}}\nabla_{\hat{c}}u^{\hat{c}}. \quad (2.14)$$

In the above, $\eta$ and $\eta_v$ represent the dynamic (shear) and volumetric (bulk) viscosities of the fluid. The thermodynamic force term $F^{\hat{a}}$ takes the following form:

$$nF^{\hat{a}} = -\phi\nabla^{\hat{a}}\mu = -\nabla^{\hat{a}}p_{\text{binary}} + \kappa\phi\nabla^{\hat{a}}\Delta\phi,$$
$$p_{\text{binary}} = A\left(-\tfrac{1}{2}\phi^2 + \tfrac{3}{4}\phi^4\right). \quad (2.15)$$

A summary on how the differential operators must be applied for the cases of the Cartesian and torus geometries is provided in Appendix C.

### C. Vielbein lattice Boltzmann approach

In this paper, we employ the lattice Boltzmann approach to solve the hydrodynamics equations [Eq. (2.13)], while the Cahn-Hilliard equation [Eq. (2.12)] is solved directly using a finite difference method. The details of the numerical implementation are discussed in Appendix C. It is possible to solve the Cahn-Hilliard equation using a lattice Boltzmann scheme, and on flat manifolds, it has been suggested that extension to more fluid components is more straightforward in this approach [43,66]. However, for our purpose here, it is more expensive than the finite difference approach.

We use a discretized form of the Boltzmann equation that reproduces the fluid equations of motion in the continuum limit. In covariant form, the Boltzmann equation on an arbitrary geometry is given by [58]

$$\frac{\partial f}{\partial t} + \frac{1}{\sqrt{g}}\frac{\partial}{\partial q^b}\left(v^{\hat{a}}e^b_{\hat{a}}f\sqrt{g}\right) + \frac{\partial}{\partial v^{\hat{a}}}\left[\left(\frac{F^{\hat{a}}}{m} - \Gamma^{\hat{a}}_{\ \hat{b}\hat{c}}v^{\hat{b}}v^{\hat{c}}\right)f\right] = J[f], \quad (2.16)$$

where $\sqrt{g}$ is the square root of the determinant of the metric tensor, and $J[f]$ is the collision operator.

For the specific case of a torus, the Boltzmann equation reads as

$$\frac{\partial f}{\partial t} + \frac{v^{\hat{\varphi}}}{R + r\cos\theta}\frac{\partial f}{\partial \varphi} + \frac{v^{\hat{\theta}}}{r(1 + a\cos\theta)}\frac{\partial[f(1 + a\cos\theta)]}{\partial\theta}$$
$$- \frac{\sin\theta}{R + r\cos\theta}\left[v^{\hat{\varphi}}\frac{\partial(fv^{\hat{\varphi}})}{\partial v^{\hat{\theta}}} - v^{\hat{\theta}}\frac{\partial(fv^{\hat{\varphi}})}{\partial v^{\hat{\varphi}}}\right]$$
$$+ \frac{F^{\hat{\varphi}}}{m}\frac{\partial f}{\partial v^{\hat{\varphi}}} + \frac{F^{\hat{\theta}}}{m}\frac{\partial f}{\partial v^{\hat{\theta}}} = J[f]. \quad (2.17)$$

The steps needed to derive Eq. (2.17) from Eq. (2.16) are summarized in Appendix A. Here, $r$ and $R$ represent the inner (small) and outer (large) radii, $a = r/R$ is the radii ratio, while the angle $\theta$ goes around the inner circle (we use the convention that the range $0 < \theta < \pi$ covers the upper side of the torus, with $\theta = 0$ corresponding to the outermost part of the torus), and $\varphi$ covers the large circle. The range for both $\theta$ and $\varphi$ is $[0, 2\pi)$ and the system is periodic with respect to both these angles. The term on the second line of Eq. (2.17) corresponds to inertial and reaction forces that arise when we have flow on curved surfaces since fluid motion is constrained on the surface.

As commonly the case in the lattice Boltzmann literature, we employ the Bhatnagar-Gross-Krook (BGK) approximation for the collision operator

$$J[f] = -\frac{1}{\tau}[f - f^{\text{eq}}], \quad (2.18)$$

where the relaxation time $\tau$ is considered to be constant. The ensuing fluid kinematic and dynamic viscosities $\nu$ and $\eta$ are [67]:

$$\nu = \frac{\eta}{\rho} = \frac{\tau k_B T}{m}. \quad (2.19)$$

Furthermore, in this paper, we only consider isothermal flows, which are implemented by constructing $f^{(eq)}$ in Eq. (2.18) with a fixed temperature. In the isothermal BGK model, the viscous stress $\sigma^{\hat{a}\hat{b}}$ is given, via the Chapman-Enskog procedure, by [68]:

$$\sigma^{\hat{a}\hat{b}} = -\eta(\boldsymbol{\nabla}^{\hat{a}}u^{\hat{b}} + \boldsymbol{\nabla}^{\hat{b}}u^{\hat{a}}). \tag{2.20}$$

Comparing the above expression with Eq. (2.14) shows that the volumetric viscosity of the isothermal BGK model for a 2D fluid is

$$\frac{\eta_v}{\rho} = \frac{\tau k_B T}{m}. \tag{2.21}$$

Rather than considering fluid distribution functions $f(\boldsymbol{v})$ with continuous velocity space $\boldsymbol{v} = (v^{\hat{\theta}}, v^{\hat{\varphi}})$, we discretize the velocity space using $\boldsymbol{v_k} = (v_{k_\theta}, v_{k_\varphi})$. The recovery of the Navier-Stokes equations requires at least a fourth order quadrature ($Q = 4$). However, in the small Mach number regime, accurate results can be obtained using the third order quadrature ($Q = 3$). The choice of quadrature is further discussed in Appendix B. Following the discretization of the velocity space, the particle number density $n$ and velocity $\boldsymbol{u}$ can be computed as zeroth and first order moments of the distribution functions

$$n = \sum_{\boldsymbol{k}} f_{\boldsymbol{k}}, \quad n\boldsymbol{u} = \sum_{\boldsymbol{k}} f_{\boldsymbol{k}} \boldsymbol{v_k}, \tag{2.22}$$

where the sum over $\boldsymbol{k} = (k_1, k_2)$ runs over the entire discrete velocity set. With the discretization of the velocity space, we also replace the Maxwell-Boltzmann equilibrium distribution with a set of distribution functions $f_{\boldsymbol{k}}^{\text{eq}}$ corresponding to the discrete velocity vectors $\boldsymbol{v_k}$. Due to the use of the vielbein formalism, the expression for $f_{\boldsymbol{k}}^{\text{eq}}$ coincides with the one employed on the flat Cartesian geometry. More details can be found in Appendix B.

## III. DRIFT DYNAMICS OF FLUID STRIPES AND DROPLETS

In this section we begin by studying the behavior of fluid stripes on the torus geometry. By minimizing the interface length subject to area conservation, we find there is a second order phase transition in the location of the equilibrium position as we vary the stripe area. In particular, we observe bistability when the stripe area exceeds a critical value. We validate the ability of our method to capture this effect in Sec. III A. We then consider the Laplace pressure test in Sec. III B. The Laplace pressure takes a different form on a torus geometry compared to that on a flat geometry, as discussed in Ref. [60]. Furthermore, the approach to equilibrium configuration through a damped harmonic motion is investigated in Sec. III C. We show that we recover the damping coefficient and the angular frequency as derived in [60]. Finally, we contrast the drift dynamics of fluid stripes with that of droplets on the torus in Sec. III D. While the former drift to the inside of the torus, the latter move to the outside of the torus.

### A. Equilibrium positions of fluid stripes

The basic idea behind establishing the equilibrium position of fluid stripes is that the interface length must attain a minimum for a fixed stripe area. We consider a stripe of angular width $\Delta\theta$, centered on $\theta = \theta_c$, such that its interfaces are located at

$$\theta_- = \theta_c - \Delta\theta/2, \quad \theta_+ = \theta_c + \Delta\theta/2. \tag{3.1}$$

As a convention, here the stripe is identified with the minority, rather than the majority, fluid component. The area $\Delta A$ enclosed between the upper and lower interfaces can be obtained as follows:

$$\Delta A = 2\pi r R \int_{\theta_-}^{\theta_+} d\theta(1 + a\cos\theta)$$
$$= 2\pi r R[\Delta\theta + 2a\sin(\Delta\theta/2)\cos\theta_c], \tag{3.2}$$

where $a = r/R$. The preservation of the area allows the variation of the stripe width $\Delta\theta$ to be related to a variation of the stripe center $\theta_c$. Setting $d\Delta A = 0$, it can be seen that

$$d\frac{\Delta\theta}{2} = \frac{a\sin(\Delta\theta/2)}{1 + a\cos(\Delta\theta/2)\cos\theta_c}\sin\theta_c d\theta_c. \tag{3.3}$$

The total interface length $\ell_{\text{total}} = \ell_+ + \ell_-$ can be computed as

$$\ell_{\text{total}} = 4\pi R\left(1 + a\cos\theta_c\cos\frac{\Delta\theta}{2}\right). \tag{3.4}$$

Imposing $d\ell_{\text{total}} = 0$ yields an equation involving the stripe width $\Delta\theta_{\text{eq}}$ and stripe center $\theta_c^{\text{eq}}$ at equilibrium

$$\left(a\cos\theta_c^{\text{eq}} + \cos\frac{\Delta\theta_{\text{eq}}}{2}\right)\sin\theta_c^{\text{eq}} = 0. \tag{3.5}$$

The above equation has different solutions depending on the stripe width. For narrow stripes, the equilibrium position is located at $\theta_c^{\text{eq}} = \pi$. There is a critical point corresponding to stripe width $\Delta\theta_{\text{eq}} = \Delta\theta_{\text{crit}} = 2\arccos(a)$, or alternatively stripe area

$$\Delta A_{\text{crit}} = 4\pi r R(\arccos a - a\sqrt{1 - a^2}). \tag{3.6}$$

For stripes with areas larger than this critical value, two equilibrium positions are possible, namely,

$$\theta_c^{\text{eq}} = \pi \pm \arccos\left[\frac{1}{a}\cos\frac{\Delta\theta_{\text{eq}}}{2}\right]. \tag{3.7}$$

We now reproduce the above phenomenon using our lattice Boltzmann approach. Unless stated otherwise, in Sec. III, we use a torus with $r = 0.8$ and $R = 2$ ($a = r/R = 0.4$). We set the parameters in our free energy model, Eq. (2.9), to $\kappa = 5 \times 10^{-4}$ and $A = 0.5$, and set the kinematic viscosity $\nu = 2.5 \times 10^{-3}$ and mobility parameter in the Cahn-Hilliard equation $M = 2.5 \times 10^{-3}$. Due to its homogeneity with respect to $\varphi$, the system is essentially one dimensional, such that a single node is used on the $\varphi$ direction (i.e., $N_\varphi = 1$). The discretization along the $\theta$ direction is performed using $N_\theta = 320$ nodes. Throughout this paper we ensure that our discretization is such that the spacing is always smaller than the interface width $\xi_0$, as given in Eq. (2.10). The time step is set to $\delta t = 5 \times 10^{-4}$.
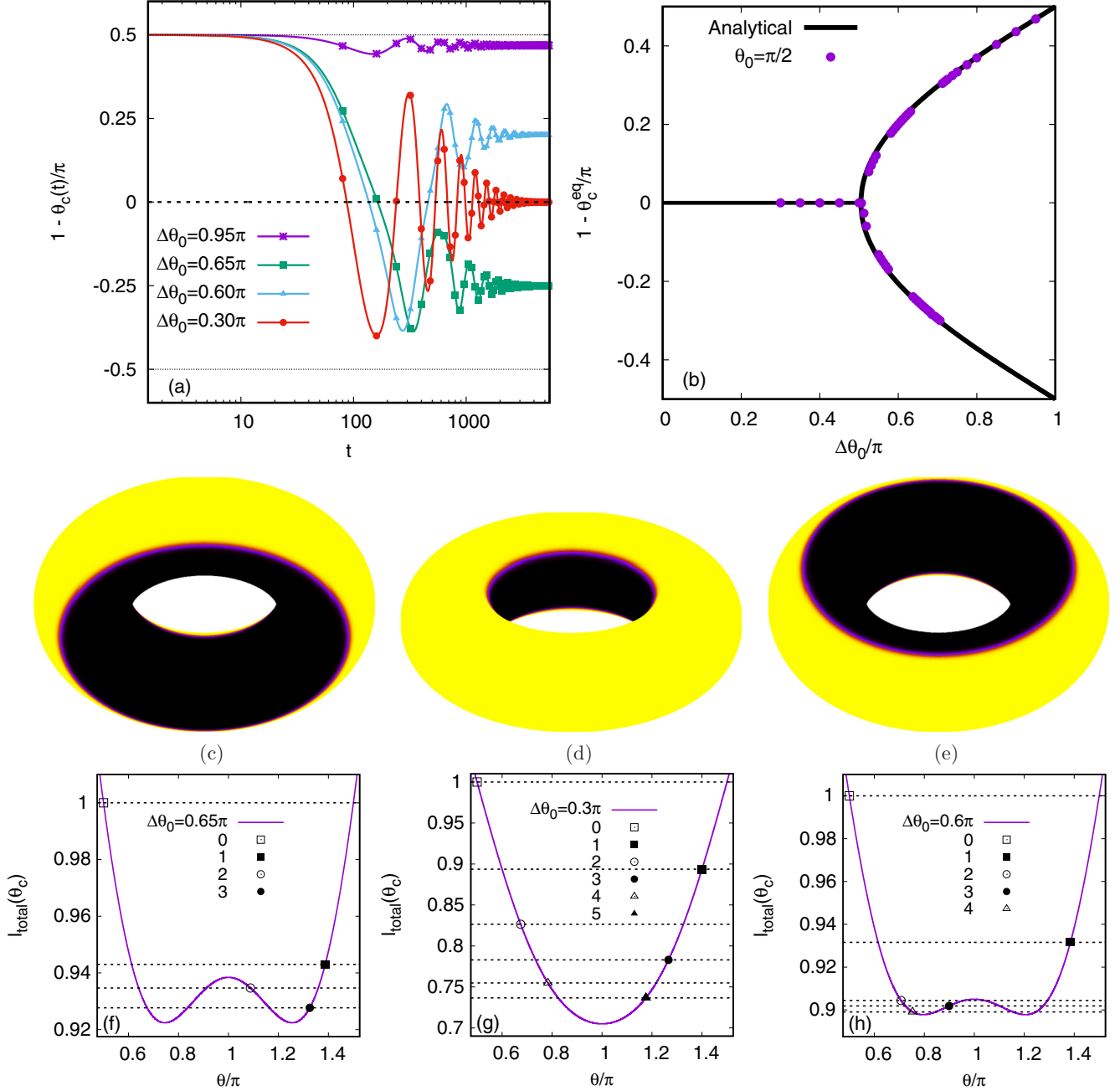
FIG. 1. (a) Time evolution of stripe center $\theta_c$ for stripes initialized at $\theta_0 = \pi/2$ on the torus with $r = 0.8$ and $R = 2$ ($a = 0.4$), with initial widths of $\Delta\theta = 0.95\pi$ ($\theta^{\text{eq}} < \pi$), $\Delta\theta = 0.65\pi$ ($\theta^{\text{eq}} > \pi$), $\Delta\theta = 0.6\pi$ ($\theta^{\text{eq}} < \pi$, with one oscillation), and $\Delta\theta = 0.3\pi$ ($\theta^{\text{eq}} = \pi$). (b) Diagram indicating the location of the equilibrium position $\theta_c^{\text{eq}}$ as a function of the stripe width $\Delta\theta_0$ and the radii ratio $a = r/R$, for stripes initialized at $\theta_0 = \pi/2$. (c)–(e) Examples of stripes equilibrated at (c) $\theta_c^{\text{eq}} > \pi$ ($\Delta\theta_0 = 0.65\pi$), (d) $\theta_c^{\text{eq}} = \pi$ ($\Delta\theta_0 = 0.3\pi$), and (e) $\theta_c^{\text{eq}} < \pi$ ($\Delta\theta_0 = 0.6\pi$). (f)–(h) Interface length $\ell_{\text{total}}$ as a function of the stripe center position (solid line) for the stripe parameters considered in (c)–(e). The symbols highlight the interface lengths at maximum oscillation amplitude at initialization (0) and after each half period (1, 2, etc.).

We initialize the fluid stripes using a hyperbolic tangent profile

$$\phi_{\text{stripe}}(\theta, t) = \phi_0 + \tanh\left[\frac{r}{\xi_0\sqrt{2}}\left(\widetilde{|\theta - \theta_c|} - \frac{\Delta\theta}{2}\right)\right], \quad (3.8)$$

where $\widetilde{\theta - \theta_c}$ gives the difference between the coordinate $\theta$ and the stripe center $\theta_c$ between $-\pi$ and $\pi$, while $\phi_0$ is an

offset due to the Laplace pressure (see next subsection)

$$\phi_0 = \frac{\xi_0}{3R\sqrt{2}}\frac{\cos\theta_c\sin(\Delta\theta/2)}{1 + a\cos\theta_c\cos(\Delta\theta/2)}. \quad (3.9)$$

We consider stripes having the same initial position centered at $\theta_0 = \pi/2$ (upper side of the torus), but initialized with different initial widths $\Delta\theta_0$. The area of these stripes is given

by

$$\Delta A = 2\pi r R \Delta\theta_0. \tag{3.10}$$

The time evolution of the stripe center $\theta_c$ for four stripes with different initial widths is shown in Fig. 1(a). The first case corresponds to a very large stripe ($\Delta\theta_0 = 0.95\pi$, $\Delta A \simeq 1.88\Delta A_{\text{crit}}$), for which the possible equilibria $\theta_c^{\text{eq}}$ are close to $\pi/2$ and $3\pi/2$. Due to the initial condition, the stripe is attracted by the equilibrium point on the upper side of the torus, where it will eventually stabilize. As the stripe size decreases, its kinetic energy as it slides toward the equilibrium point will be sufficiently large for it to go over the "barrier" at $\theta_c = \pi$ to the lower side of the torus. Because of energy loss due to viscous dissipation, its kinetic energy may be insufficient to overcome this barrier again, so the stripe remains trapped on the lower side. This is the case for the second stripe having $\Delta\theta_0 = 0.65\pi$ ($\Delta A \simeq 1.29\Delta A_{\text{crit}}$). Further decreasing the stripe size causes the peak at $\theta_c = \pi$ to also decrease, allowing the stripe to overcome the barrier a second time as it migrates back toward the upper side. The third stripe, initialized with $\Delta\theta_0 = 0.6\pi$ ($\Delta A \simeq 1.19\Delta A_{\text{crit}}$), stabilizes on the upper side of the torus. Finally, the fourth stripe is initialized with $\Delta\theta_0 = 0.3\pi$, such that its area $\Delta A \simeq 0.59\Delta A_{\text{crit}}$ is below the critical value. Thus, the fourth stripe will perform oscillations around the equilibrium at $\theta_c = \pi$, where it will eventually stabilize.

Judging by the number of times that the stripe center $\theta_c$ crosses the barrier at $\theta_c = \pi$, two types of stripes having $\Delta A > \Delta A_{\text{crit}}$ can be distinguished: (i) the ones that cross the $\theta_c = \pi$ line an even number of times stabilize on the upper side of the torus, while (ii) the ones that cross it an odd number of times stabilize on the lower side of the torus. This is presented in Fig. 1(b), where the equilibrium position $\theta_c^{\text{eq}}$ for stripes initialized at $\theta_0 = \pi/2$ is represented as a function of $\Delta\theta_0$ in comparison with the analytical predictions in Eq. (3.7).

Figures 1(c)–1(e) illustrate the three scenarios where the stripes are equilibrated at $\theta_c^{\text{eq}} > \pi$, $\theta_c^{\text{eq}} = \pi$, and $\theta_c^{\text{eq}} < \pi$, respectively. The total interface lengths $\ell_{\text{total}}$ ($\sim\Psi$) for the stripes shown in Figs. 1(c)–1(e) are represented in Figs. 1(f)–1(h). The interface lengths corresponding to the initial state, as well as to the turning points corresponding to half-periods, are also shown using symbols, numbered sequentially in the legend (0 corresponds to the initial state). It can be seen that $\ell_{\text{total}}$ measured at these turning points decreases monotonically. When $\ell_{\text{total}}$ decreases below its value at $\theta_c = \pi$, the stripe center can no longer cross the $\theta_c = \pi$ line and becomes trapped in one of the minima.

Figure 2 further summarizes the location of the equilibrium stripe position as a function of the stripe width $\Delta\theta_0$ and the radii ratio $a = r/R$. Our simulations are performed by keeping $R = 2$ constant, such that the various values of $a$ are obtained by changing $r$. As before, the stripe is initialized at $\theta_0 = \pi/2$. Moving from the top right corner of the diagram toward the bottom left corner, the subsequent regions distinguish between whether the stripes stabilize on the upper side ($<\pi$) or on the lower side ($>\pi$) of the torus, depending on the number of times that $\theta_c$ crosses $\pi$. In the bottom left corner, the stripes stabilize at $\theta_c^{\text{eq}} = \pi$. The black region between the purple band and the lower left region correspond to stripes that cross $\pi$ more than three times but stabilize away from $\pi$ ($\theta_c^{\text{eq}} \neq \pi$).
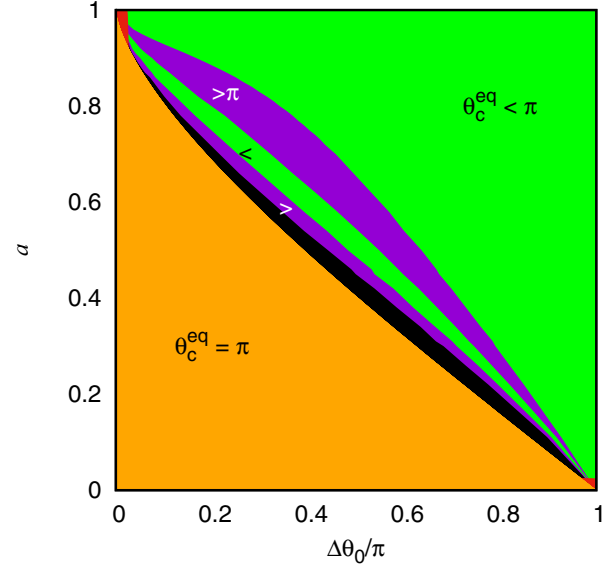


FIG. 2. Diagram indicating the location of the equilibrium position $\theta_c^{\text{eq}}$ as a function of the stripe width $\Delta\theta_0$ and the radii ratio $a = r/R$, for stripes initialized at $\theta_0 = \pi/2$.

Due to the diffuse nature of the interface, the stripes evaporate when $r\Delta\theta \lesssim 5\xi_0$ ($\xi_0 = \sqrt{\kappa/A} \simeq 0.031$). These regions correspond to the top left and bottom right corners of the diagram and are shown in red.

### B. Laplace pressure test

Since the stripe interfaces have a nonvanishing curvature, it can be expected that there will be a pressure difference across this interface. This pressure difference is often termed
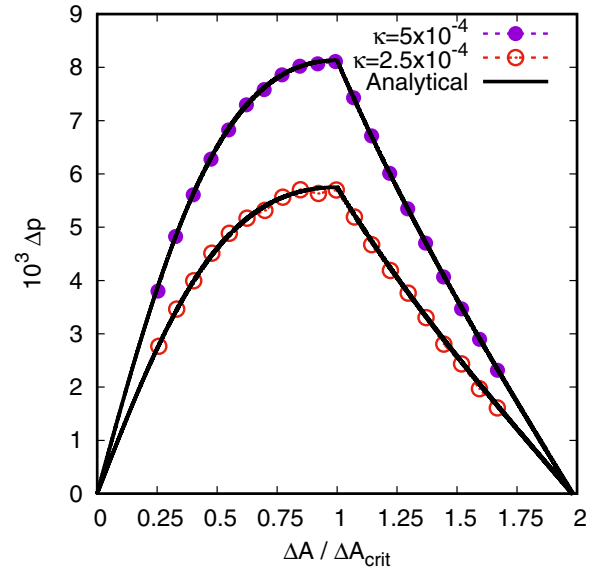


FIG. 3. Comparison of the Laplace pressure obtained numerically (dashed lines and circles) against the analytic formula (3.12) for $\kappa = 5 \times 10^{-4}$ (dotted lines and filled circles) and $2.5 \times 10^{-4}$ (dotted lines and empty circles). The analytic predictions (solid black lines) are almost everywhere overlapped with the numerical results.

the Laplace pressure, and it was recently derived analytically on a tors. The result is [60]

$$\Delta p = -\frac{\gamma}{R} \frac{\cos\theta_c \sin(\Delta\theta/2)}{1 + a \cos\theta_c \cos(\Delta\theta/2)}. \quad (3.11)$$

This expression can be simplified for the two types of equilibrium positions highlighted in the previous subsection:

$$\Delta p = \begin{cases} \frac{\gamma}{R} \frac{\sin(\Delta\theta_{eq}/2)}{1 - a\cos(\Delta\theta_{eq}/2)}, & \Delta A < \Delta A_{crit}, \\ \frac{\gamma}{r} \cot\frac{\Delta\theta_{eq}}{2}, & \Delta A > \Delta A_{crit}. \end{cases} \quad (3.12)$$

We remind the readers that, on the first branch, $\theta_c^{eq} = \pi$. On the second branch, the equilibrium position is determined via $a\cos\theta_c^{eq} + \cos(\Delta\theta_{eq}/2) = 0$.

In order to validate our numerical scheme against the Laplace pressure test on the torus, we perform numerical simulations for two values of $\kappa$ in our free energy model $\kappa = 2.5 \times 10^{-4}$ and $5 \times 10^{-4}$. These effectively change the surface tension and interface width in our simulations [see Eq. (2.10)]. All of the other simulation parameters are kept the same as in the previous subsection: $R = 2$, $r = 0.8$, $A = 0.5$, $\nu = 2.5 \times 10^{-3}$, and $M = 2.5 \times 10^{-3}$. We consider stripes of various areas $\Delta A$ in Fig. 3. After the stationary state is reached, we measure the total pressure $p = p_i + p_{binary} = nk_BT + A(-\frac{1}{2}\phi^2 + \frac{3}{4}\phi^4)$ in the interior and exterior of the stripe, and compute the difference $\Delta p$ between these two values. The simulation results are shown using dashed lines and symbols in Fig. 3. We observe an excellent agreement with the analytic results, Eq. (3.12), which are shown using the solid lines.

### C. Approach to equilibrium

For stripes close to their equilibrium position, the time evolution of the departure $\delta\theta = \theta_c - \theta_c^{eq}$ can be described as a damped harmonic oscillation:

$$\delta\theta \simeq \delta\theta_0 \cos(\omega_0 t + \varsigma)e^{-\alpha t}, \quad (3.13)$$

where the damping coefficient $\alpha = \alpha_\nu + \alpha_\mu$ receives contributions from the viscous damping due to the fluid [60]

$$\alpha_\nu = \frac{\nu}{R^2 - r^2}, \quad (3.14)$$

as well as from the diffusion due to the mobility of the order parameter $\alpha_\mu$ [60]. In the applications considered in this paper, $\alpha_\mu \ll \alpha_\nu$, such that we will only consider the approximation $\alpha \simeq \alpha_\nu$. For the case of subcritical stripes ($\Delta A < \Delta A_{crit}$), which equilibrate at $\theta_c^{eq} = \pi$, the oscillation frequency is [60]

$$\omega_0^2 = \frac{\gamma\sqrt{1 - a^2}}{\pi r^2 R\rho} \frac{\cos(\Delta\theta_{eq}/2) - a}{[1 - a\cos(\Delta\theta_{eq}/2)]^3}. \quad (3.15)$$

For the supercritical stripes ($\Delta A > \Delta A_{crit}$), when the equilibrium position is at $a\cos\theta_c^{eq} + \cos(\Delta\theta_{eq}/2) = 0$, $\omega_0^2$ is given by

$$\omega_0^2 = \frac{2\gamma}{\pi r R^2 \rho (1 - a^2)^{3/2}} \left[\frac{\sin\theta_c^{eq}}{\sin(\Delta\theta_{eq}/2)}\right]^2. \quad (3.16)$$

We will now demonstrate that our lattice Boltzmann implementation captures the dynamical approach to equilibrium as described by the analytical results. First, we consider a torus
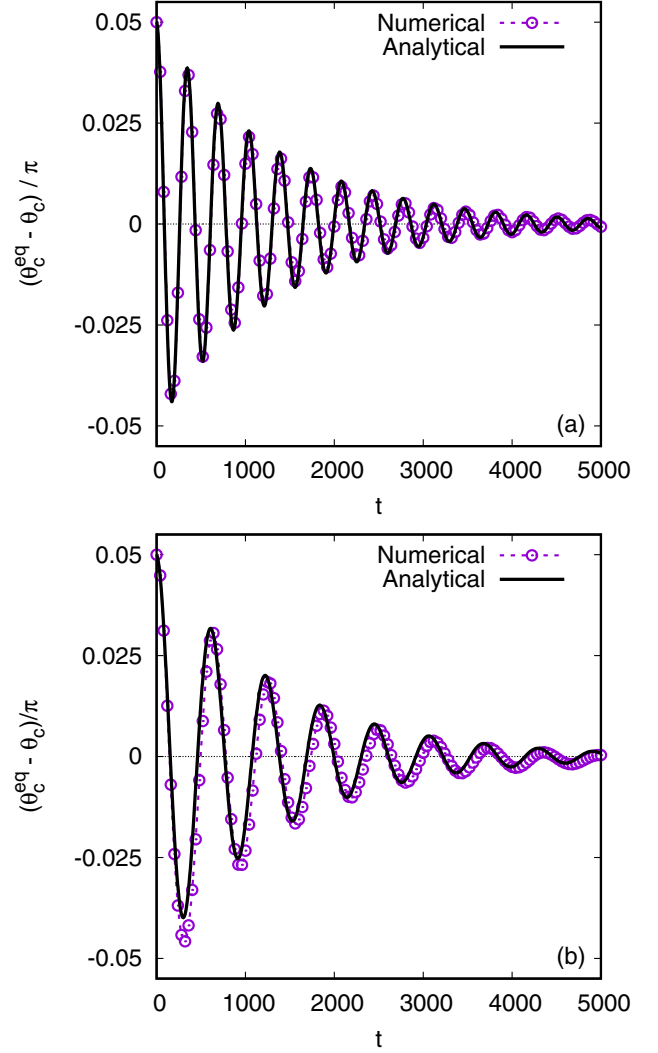


FIG. 4. Time evolution of the stripe center $\theta_c$ for stripes initialized at (a) $\theta_0 = 0.95\pi$ with $\Delta\theta_0 = 0.280\pi$ (equilibrating at $\theta_c^{eq} = \pi$) and (b) $\theta_0 = 0.7\pi$ with $\Delta\theta_0 = 0.796\pi$ (equilibrating at $\theta_c^{eq} = 3\pi/4$). The numerical results are shown using dotted lines and symbols, while the analytic solutions are shown using solid lines.

with $r = 0.8$ and $R = 2$ ($a = 0.4$), and set $\kappa = 5 \times 10^{-4}$, $A = 0.5$, and $\tau = M = 2.5 \times 10^{-3}$. The number of nodes is $N_\theta = 320$, and the order parameter $\phi$ is initialized according to Eq. (3.8), where the stripe center is located at an angular distance $\delta\theta_0 = \theta_c - \theta_c^{eq} = -\pi/20$ away from the expected equilibrium position. Figure 4 shows a comparison between the numerical and analytical results for the time evolution of $(\theta_c^{eq} - \theta_c)/\pi$ for the cases (a) $\theta_c^{eq} = \pi$ with initial stripe width $\Delta\theta_0 = 0.28\pi$ and (b) $\theta_c^{eq} = 3\pi/4$ with $\Delta\theta_0 = 0.786\pi$. For the analytical solution, the angular velocity $\omega_0$ is computed using Eqs. (3.15) and (3.16) for cases (a) and (b), respectively, and the damping factor $\alpha \simeq \alpha_\nu$ is computed using Eq. (3.14). We also set $\varsigma = 0$ in Eq. (3.13). It can be seen that the simulation results are in excellent agreement with the analytic expression for the stripe that goes to $\theta_c^{eq} = \pi$. For the stripe equilibrating to $3\pi/4$, we observe a small discrepancy, especially during the first oscillation period. However, the overall agreement is still very good.
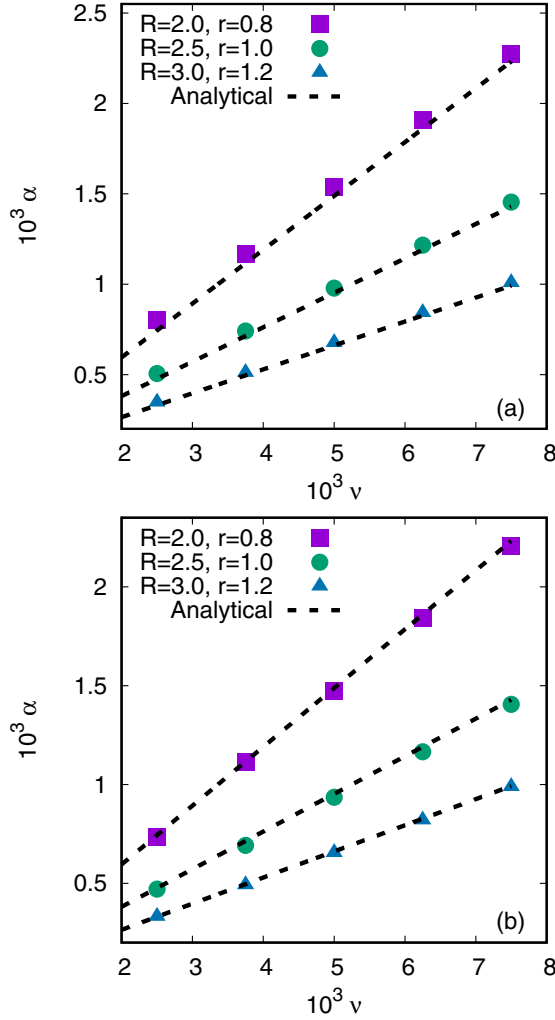
FIG. 5. The damping coefficient $\alpha$ obtained by fitting Eq. (3.13) to the simulation results (points), for stripes initialized at (a) $\theta_0 = 0.95\pi$ with $\theta_c^{eq} = \pi$ and (b) $\theta_0 = 0.7\pi$ with $\theta_c^{eq} = 0.75\pi$. The dashed lines represent the viscous damping coefficient $\alpha_\nu$, given in Eq. (3.14).
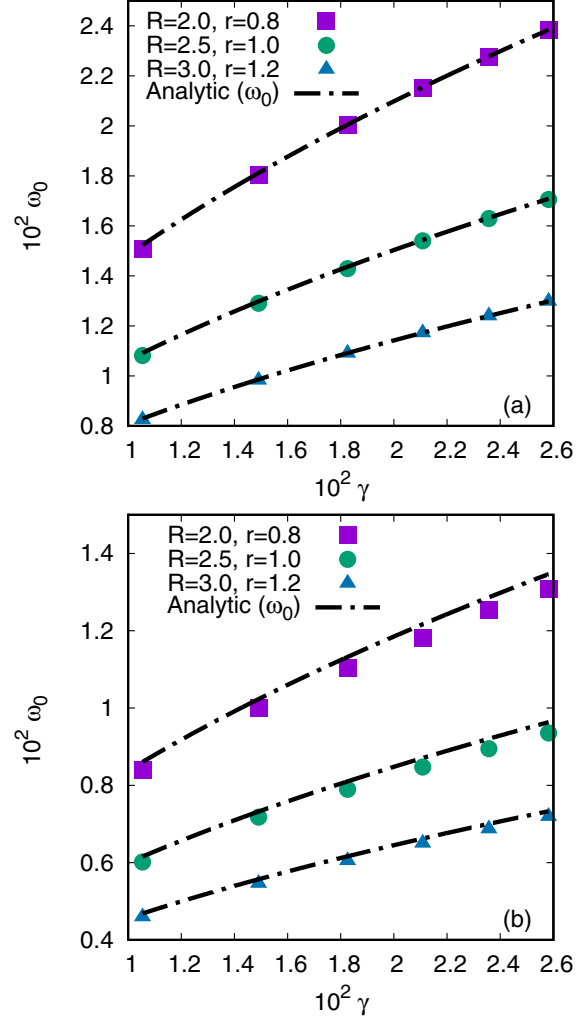


FIG. 6. The angular frequency $\omega_0$, obtained by fitting Eq. (3.13) to the simulation results (points). The black dashed-dotted curves correspond to the analytic expressions, as given by Eq. (3.15) for (a), when $\theta_c^{eq} = \pi$ and Eq. (3.16) for (b), when $\theta_c^{eq} = 3\pi/4$.

Next, we consider three tori having radii ratio $a = r/R = 0.4$, with $r = 0.8$, 1, and 1.2, and perform two sets of simulations. In the first set of simulations, the initial configuration corresponds to a stripe centered on $\theta_0 = 0.95\pi$, with initial width $\Delta\theta_0 = 0.28\pi$. These stripes relax toward $\theta_c^{eq} = \pi$. In the second set of simulations, the stripes are initially centered at $\theta_0 = 0.7\pi$, and they equilibrate at $\theta_c^{eq} = 3\pi/4$, with initial width $\Delta\theta_0 = 0.786\pi$. The simulations are performed using $N_\theta = 320$, 400, and 480 nodes for $r = 0.8$, 1, and 1.2, respectively. The best-fit values of $\alpha$ and $\omega_0$ for the three torus geometries are shown in Figs. 5 and 6, respectively, as functions of the kinematic viscosity $\nu$ (varying between $2.5 \times 10^{-3}$ and $7.5 \times 10^{-3}$) at $\kappa = 5 \times 10^{-4}$ and of the line tension $\gamma = \sqrt{8\kappa A/9}$ ($A = 0.5$ is kept fixed and $\kappa$ is varied between $2.5 \times 10^{-4}$ and $1.5 \times 10^{-3}$) at $\nu = 2.5 \times 10^{-3}$. For each simulation, Eq. (3.13) is fitted to the numerical data for the time evolution of the stripe center as it relaxes toward equilibrium, using $\alpha$ and $\omega$ as free parameters, while $\varsigma = 0$. For simplicity, we used $M = \nu$ and $A = 0.5$ in Figs. 5

and 6. Figures 5(a) and 6(a) correspond to stripes equilibrating at $\theta_c^{eq} = \pi$, while Figs. 5(b) and 6(b) are for $\theta_c^{eq} = 3\pi/4$. It can be seen that the analytic expressions are in good agreement with the numerical data in all instances simulated.

Finally, we investigate the applicability of Eqs. (3.15) and (3.16) with respect to various values of the stripe area $\Delta A$. The simulations are now performed on the torus with $r = 0.8$ and $R = 2$, using $\kappa = 5 \times 10^{-4}$, $A = 0.5$, $\tau = M = 2.5 \times 10^{-3}$. Figure 7 shows the values of $\omega_0$ obtained by fitting Eq. (3.13) to the numerical data (points) and the analytic expressions (solid lines). As before, for the fitting, we set $\varsigma = 0$, and use $\alpha$ and $\omega_0$ as free parameters. An excellent agreement can be seen, even for the nearly critical stripe, for which $\omega_0$ is greatly decreased.

### D. Droplets on tori

We will now show that, when placed on a torus, a fluid droplet will also exhibit a drift motion. However, in contrast to stripes, the drops will move toward the outer rather than
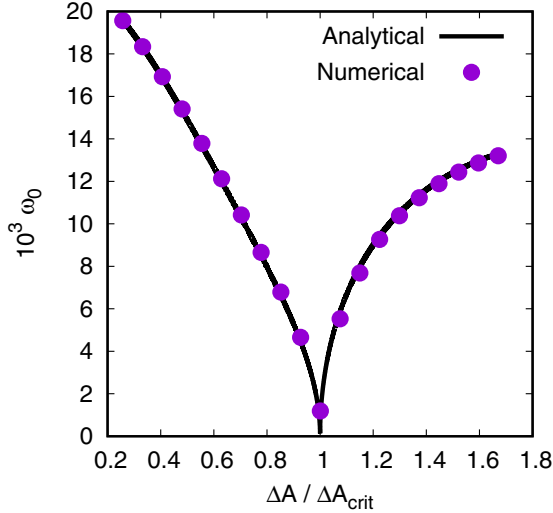
FIG. 7. Comparison between the values of $\omega_0$ obtained by fitting Eq. (3.13) to the numerical results, shown with points, and the analytic expressions (3.15) for $\Delta A < \Delta A_{\rm crit}$ and (3.16) for $\Delta A > \Delta A_{\rm crit}$, shown with solid black lines.

the inner side of the torus. To study this phenomenon quantitatively, we initialize drops on a torus using the following equation:

$$\phi_{\rm drop}(\theta_0, R_0; \theta, \varphi) = \tanh \frac{r - R_0}{\xi_0 \sqrt{2}}, \qquad (3.17)$$

where $r = \sqrt{(x - x_c) + (y - y_c) + (z - z_c)}$ is the Euclidean distance between the point with coordinates $(x, y, z)$ and the center of the drop $(x_c, y_c, z_c)$, corresponding to $(\theta, \varphi)$ and $(\theta_0, 0)$ in polar coordinates, respectively. The relation between the Cartesian and polar coordinates is given in Eq. (A1) of Appendix A. The parameter $\theta_0$ represents the center of the drop, while $R_0$ is a measure of its radius. $\xi_0$ is the interface width derived for the Cartesian case. In principle, the interfacial profile will be different on a torus, but currently we are not aware of a closed analytical formula. We also do not introduce in Eq. (3.17) the offset $\phi_0$ responsible for the Laplace pressure difference since the analysis of this quantity is less straightforward than for the azimuthally symmetric stripe domains discussed in the previous subsections.

In order for the drops to have approximately the same areas, for a given value of $\theta_0$, $R_0$ is obtained as a solution of

$$\int_0^{2\pi} d\varphi \int_0^{2\pi} d\theta (R + r \cos \theta)[\phi_{\rm drop}(0, 30\xi_0; \theta, \varphi) - \phi_{\rm drop}(\theta_0, R_0; \theta, \varphi)] = 0, \qquad (3.18)$$

where the first term in the parentheses corresponds to the configuration when the droplet is centered on the outer equator and has $R_0 = 30\xi_0$. The drift phenomenon we report here is robust with respect to the drop size, but we choose a relatively large drop size because small drops are known to evaporate in diffuse interface models. The simulation parameters are the same as in Sec. III C, namely, $r = 0.8$, $R = 2$, $\kappa = 5 \times 10^{-4}$, $A = 0.5$, and $\tau = M = 2.5 \times 10^{-3}$.

As shown in Fig. 8(a), similar to the stripe configuration in the previous subsection, we observe a damped oscillatory

motion. Here, the three drops are initialized at different positions on the torus. Moreover, as is commonly the case for an underdamped harmonic motion, the drops initially overshoot the stable equilibrium position, but they eventually relax to the minimum energy configuration. In all cases considered in this section, we find that the drops eventually drift to $\theta = 0$ (the outer side of the torus). Typical drop configurations during the oscillatory motion are shown in Figs. 8(b)–8(d). Compared to the oscillatory dynamics for the stripe configurations, we also observe that the oscillation dies out quicker for the drops.

## IV. PHASE SEPARATION

In this section we investigate binary phase separation on the torus and compare the results against those on flat surfaces. We consider hydrodynamics and diffusive regimes for both even (Sec. IV A) and uneven (Sec. IV B) mixtures.

The fluid order parameter at lattice point $(s, q)$ is initialized as

$$\phi_{s,q} = \overline{\phi} + (\delta\phi)_{s,q}, \qquad (4.1)$$

where $\overline{\phi}$ is a constant and $(\delta\phi)_{s,q}$ is randomly distributed between $(-0.1, 0.1)$. We characterize the coarsening dynamics using the instantaneous domain length scale $L_d(t)$, computed using the following function:

$$L_d(t) = \frac{A_{\rm total}}{L_I(t)}, \qquad (4.2)$$

where $A_{\rm total}$ is the total area of the simulation domain. The total interface length at time $t$, $L_I(t)$, is computed by visiting each cell $(s, q)$ exactly once, starting from the bottom left corner, where $s = q = 1$, and progressing toward the top right corner, where $s = N_1$ and $q = N_2$. $N_1 = N_x$ and $N_2 = N_y$ for the Cartesian domains and $N_1 = N_\varphi$ and $N_2 = N_\theta$ for the torus domains. For each cell where $\phi_{s,q} \times \phi_{s+1,q} < 0$, the length of the vertical interface between the $(s, q)$ and $(s + 1, q)$ cells is added to $L_I$. In the case of the Cartesian geometry, this length is $\delta y$, while for the torus, the length is given by $r\delta\theta$. Similarly, if $\phi_{s,q} \times \phi_{s,q+1} < 0$, the length of the horizontal interface [$\delta x$ for the Cartesian case and $(R + r \cos \theta_{q+1/2})\delta\varphi$ for the torus case, where $\theta_{q+1/2} = \theta_q + \delta\theta/2$ is the coordinate of the cell interface] is added to $L_I$. The periodic boundary conditions allow the cells with $(N_1 + 1, q)$ and $(s, N_2 + 1)$ to be identified with the cells $(1, q)$ and $(s, 1)$, respectively.

Unless specified otherwise, we use the following parameters in this phase separation section: $M = \tau = 2.5 \times 10^{-3}$, $\delta t = 5 \times 10^{-4}$, $A = 0.5$, and $\kappa = 5 \times 10^{-4}$. In the initial state, the distributions for the LB solver are initialized using Eq. (B26) with a constant density $n_0 = 20$ and vanishing velocity.

### A. Even mixtures

#### 1. Cartesian geometry

We begin by considering the coarsening dynamics of a phase separating binary fluid with even mixtures on a flat two-dimensional surface. We use a simulation domain of $N_x \times N_y = 512 \times 512$ with a grid spacing of $\delta x = \delta y = 0.02$. The linear size of the simulation domain is $L = 512 \times 0.02 = 10.24$ and its total area is $A_{\rm total} = L^2$.
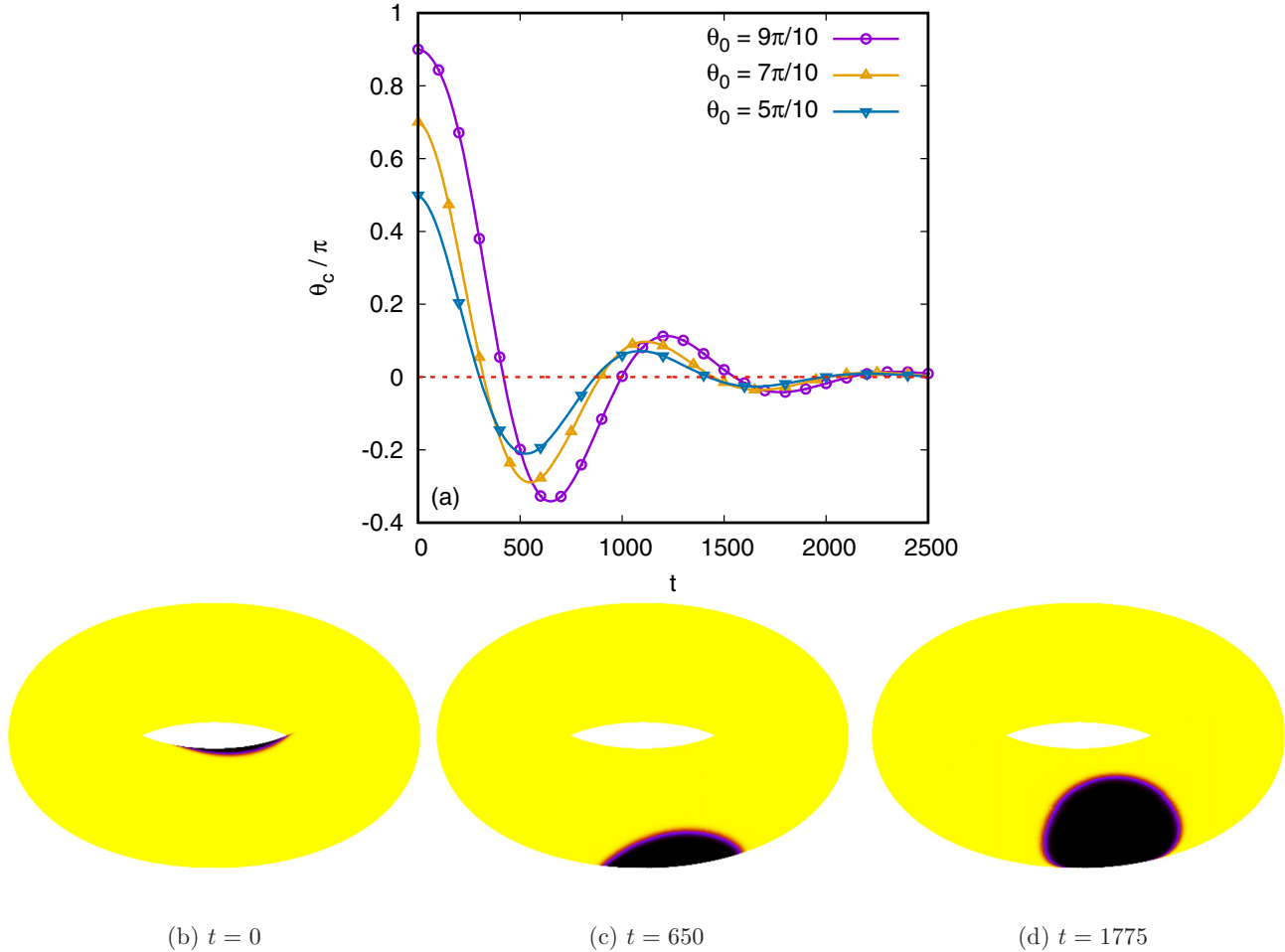
(b) $t = 0$           (c) $t = 650$           (d) $t = 1775$

FIG. 8. (a) Time evolution of the position of the center $\theta_c/\pi$ for drops initialized according to Eq. (3.17) with $(\theta_0, R_0) \in \{(5\pi/10, 0.938), (7\pi/10, 0.924), (9\pi/10, 0.910)\}$. (b)–(d) Snapshots of the evolution of the drop corresponding to $\theta_0 = 9\pi/10$ for $t = 0$, 650, and 1775.

As shown in Fig. 9(a), we observe that the fluid domain grows with an exponent of $\frac{2}{3}$. This exponent is often associated with the so-called inertial-hydrodynamics regime for binary fluid phase separation in three dimensions [61,62]. However, in two dimensions, it has been argued that self-similar growth in the inertial-hydrodynamics regime may be absent [63]. The apparent exponent of $\frac{2}{3}$ is really due to a mixture of viscous exponent of 1 for the growth of the connected domains and an exponent of $\frac{1}{3}$ for the diffusive dissolution of circular droplets.

Classical morphologies typical of a spinodal decomposition phenomenon are shown in Figs. 9(c)–9(f). The deviation from this apparent scaling law is observed at early times when the domains of fluid components A and B are formed from the initial perturbation, and at late times, due to *finite size effects*, when the domains become comparable in size to the simulation box. For the latter, there are very few domains left [see Fig. 9(f)], and coarsening slows down because of the lack of coalescence events between the fluid domains.

To access the diffusive regime, in this work we remove the advection term in the Cahn-Hilliard equation and decouple it from the Navier-Stokes equation. In this case, coarsening can only occur via diffusive dynamics, and indeed we do observe a growth exponent of $\frac{1}{3}$, as shown in Fig. 9(b), as expected

for diffusive dynamics [61,62]. Representative configurations from the coarsening evolution are shown in Figs. 9(g)–9(j). These snapshots look somewhat similar to those shown in Figs. 9(c)–9(f) for the apparent $\frac{2}{3}$ scaling regime. The key difference between the morphologies is that more small droplets are accumulated during coarsening when hydrodynamics is on. It is also worth noting that the coarsening dynamics are much slower in the diffusive regime. At late times we see a deviation from the diffusive scaling exponent, where $L_d(t)$ appears to grow faster than $\frac{1}{3}$ exponent. In this limit, as illustrated in Fig. 9(j), the increase in $L_d(t)$ is primarily driven by finite size effects.

### 2. Torus geometry

We now consider the coarsening dynamics of a phase separating binary fluid on the surface of a torus. Initially, we simulate a torus domain with $R = 2.5$ and $r = 1$ ($a = r/R = 0.4$). These parameters are chosen such that the total area $A_{\text{total}} = 4\pi^2 rR$ is close to the one employed in the Cartesian case. The $\varphi$ direction is discretized using $N_\varphi = 800$ nodes, while the $\theta$ direction is discretized using $N_\theta = 400$ nodes. The fluid order parameter at lattice point $(s, q)$ is initialized according to Eq. (4.1) with $\overline{\phi} = 0$.
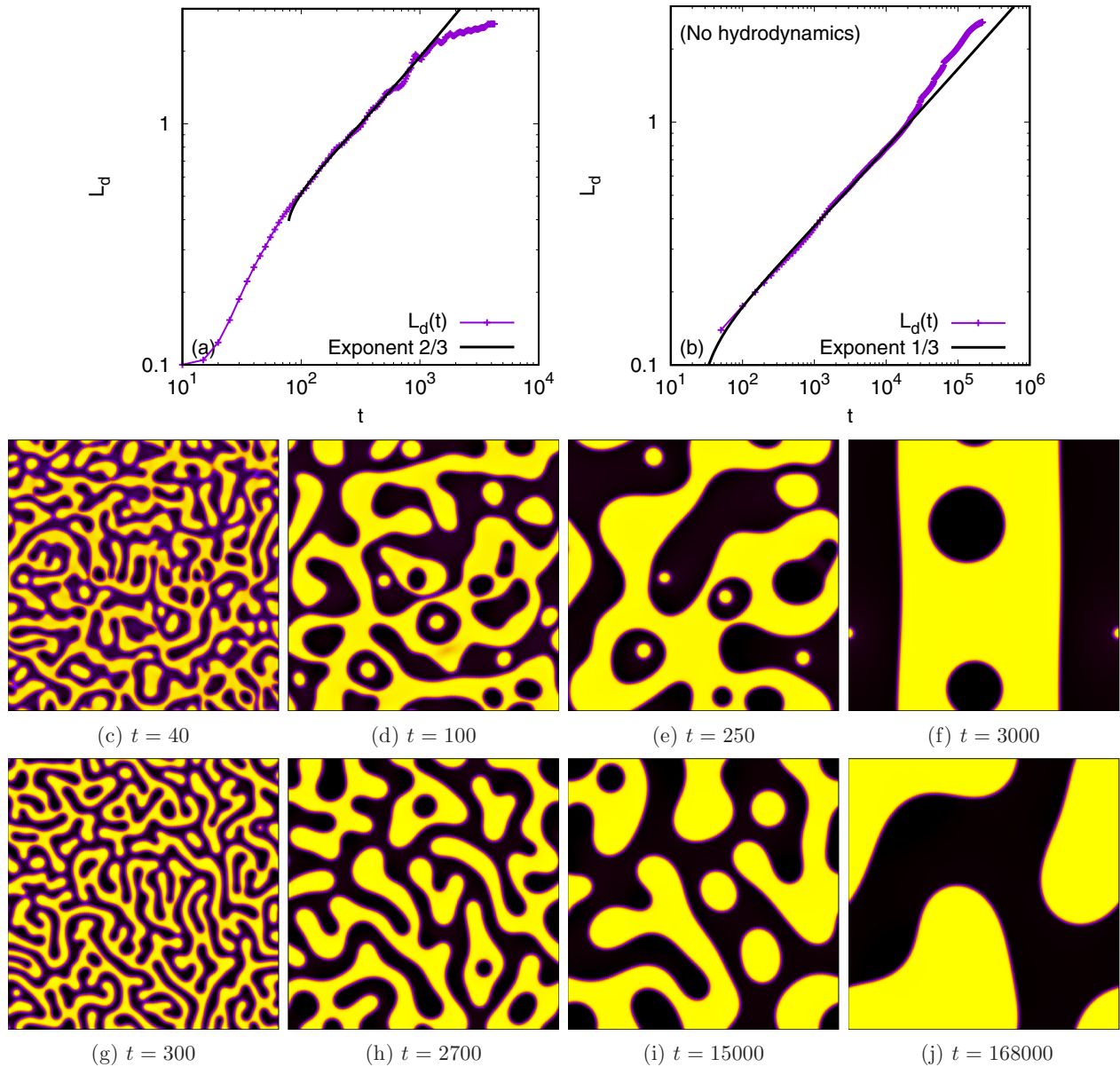
FIG. 9. Growth of the fluid domain size $L_d(t)$ for an even mixture in two dimensions in (a) the inertial-hydrodynamics and (b) the diffusive regimes. For the diffusive regime, we remove the convective term in the Cahn-Hilliard equation. (c)–(f) Snapshots of the typical fluid configurations at $t = 40$, 100, 250, and 3000 corresponding to the case indicated in (a). (g)–(j) Snapshots of the fluid configurations corresponding to the case indicated in (b), at times $t = 300$, 2700, 15 000, and 168 000. These are selected such that $L_d(t)$ matches the values corresponding to (c)–(f).

Our simulation results are shown in Figs. 10(a) and 10(b), respectively, for cases with and without coupling to hydrodynamics. Qualitatively, we find a similar behavior to the results obtained in the Cartesian case, Fig. 9. In Fig. 10(a), it can be seen that $L_d(t)$ grows with an apparent exponent of $\frac{2}{3}$ when hydrodynamics is on. Turning off the hydrodynamics, the $\frac{1}{3}$ diffusive exponent emerges, as demonstrated in Fig. 10(b). The coarsening dynamics is also much faster with hydrodynamics on the torus. Snapshots of the order parameter configuration at various times for the case of the even mixture with and without hydrodynamics are shown in Figs. 10(c)–10(e) and 10(f)–10(h), respectively.

Quantitatively, we observe that finite size effects occur earlier (smaller $L_d$) for the torus considered in Fig. 10 compared to the Cartesian case. This is expected since the effective length scale in the poloidal direction $2\pi r$ is smaller than the width of the simulation box in the Cartesian case, even though the total surface areas are comparable. Indeed, we can observe that the departure from the $\frac{2}{3}$ [Fig. 10(a)] and $\frac{1}{3}$ [Fig. 10(b)] exponents occur when the fluid domains start to wrap around the circle in the poloidal direction.

In Fig. 11 we further show simulation results for a thicker ($R = 2$ and $r = 1.25$; $a = 0.625$) and a thinner ($R = 5$ and $r = 0.5$; $a = 0.1$) torus, having a total area equal to the one considered at the beginning of this section. The simulation
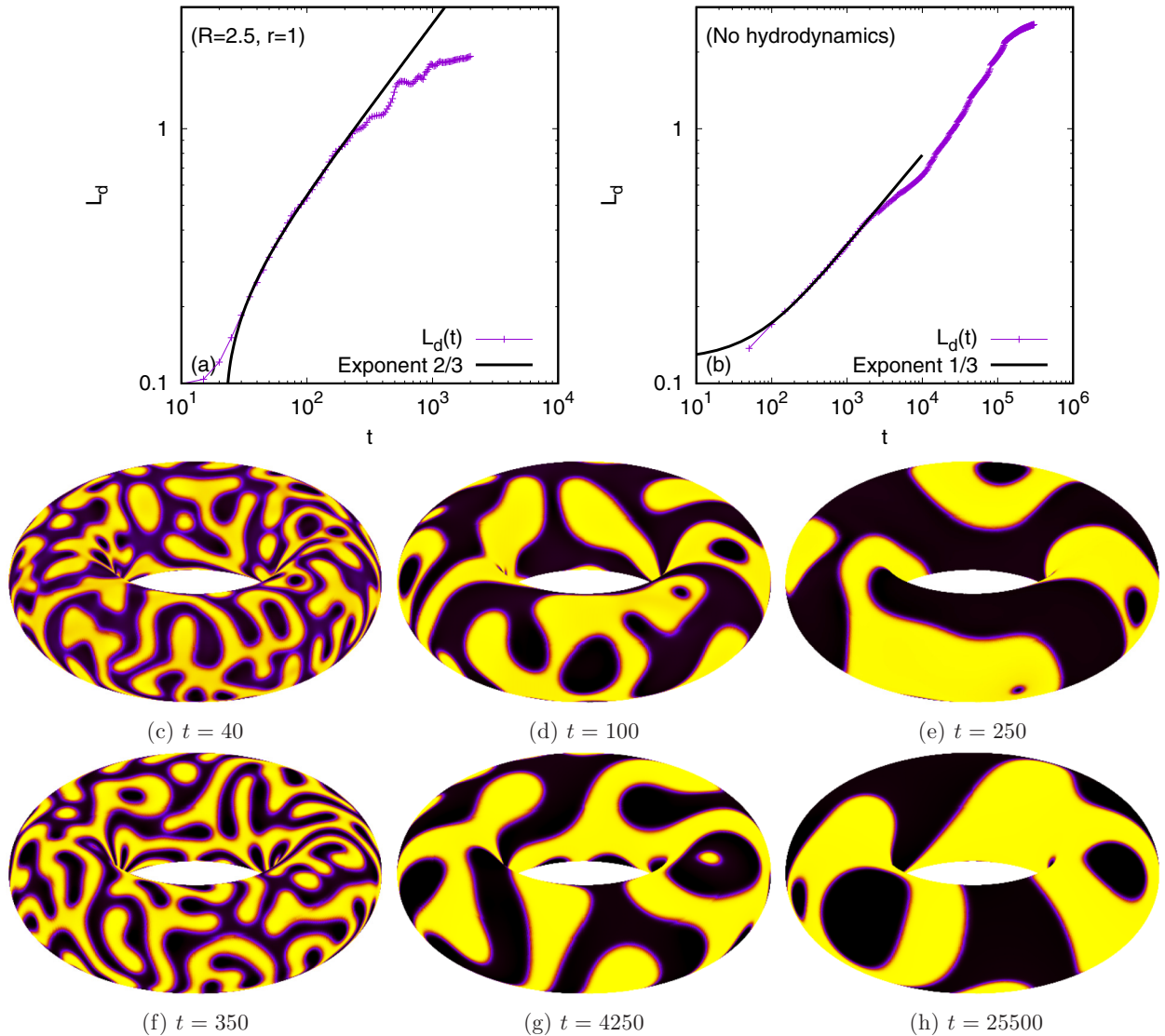
FIG. 10. Growth of the fluid domain size $L_d(t)$ for an even mixture on the surface of a torus with $R = 2.5$ and $r = 1$ in (a) the inertial-hydrodynamics and (b) the diffusive regimes. For the diffusive regime, the convective term in the Cahn-Hilliard equation is removed. (c)–(e) Snapshots of the typical fluid configurations at $t = 40$, $100$, and $250$ corresponding to the case indicated in (a). (f)–(h) Snapshots of the typical fluid configurations at $t = 350$, $4250$, and $25\,500$ corresponding to the case indicated in (b). The times are chosen such that the values of $L_d$ match the ones corresponding to (c)–(e).

parameters are kept the same as before, except that for the thicker torus, the time step must be decreased down to $\delta t = 5 \times 10^{-5}$ since the minimum spacing along the $\varphi$ direction occurring on the inner equator is $2\pi(R - r)/N_\varphi \sim 0.00589$. Comparing Figs. 10(a), 11(a), and 11(b), finite size effects seem to appear sooner for the thinner torus and later for the thicker torus, which suggests the importance of the circumference in the poloidal direction for finite size effects. An interesting direction for future work would be to systematically study how finite size effects are influenced by the interplay between the circumference in the poloidal direction, $2\pi r$, and the circumference on the inner side of the torus (at $\theta = \phi$), $2\pi(R - r)$.

Given the fluid stripes are generally formed in the poloidal rather than the toroidal direction during phase separation, the drift phenomenon reported in Sec. III C for stripe configurations cannot be clearly visualized. However, domain drifts for

drops, as reported in Sec. III D, can be seen in Figs. 10 and 11 during the late stages of the coarsening phenomenon. This drift phenomenon can be observed even clearer when we study uneven mixtures, as discussed in the next section.

### B. Uneven mixtures

#### 1. Cartesian geometry

The simulation results for a mixture with asymmetric composition are shown in Fig. 12. We use the same simulation parameters as in Fig 9, except that $\overline{\phi} = -0.3$. Figure 12(a) shows how the typical domain size scales with time both when hydrodynamics is turned on and off. Interestingly, in both cases we observe an exponent of $\frac{1}{3}$, albeit with different prefactors. This is in contrast to our results for the even mixtures, when an apparent exponent of $\frac{2}{3}$ is obtained with hydrodynamics. It has been suggested in the literature that the effect
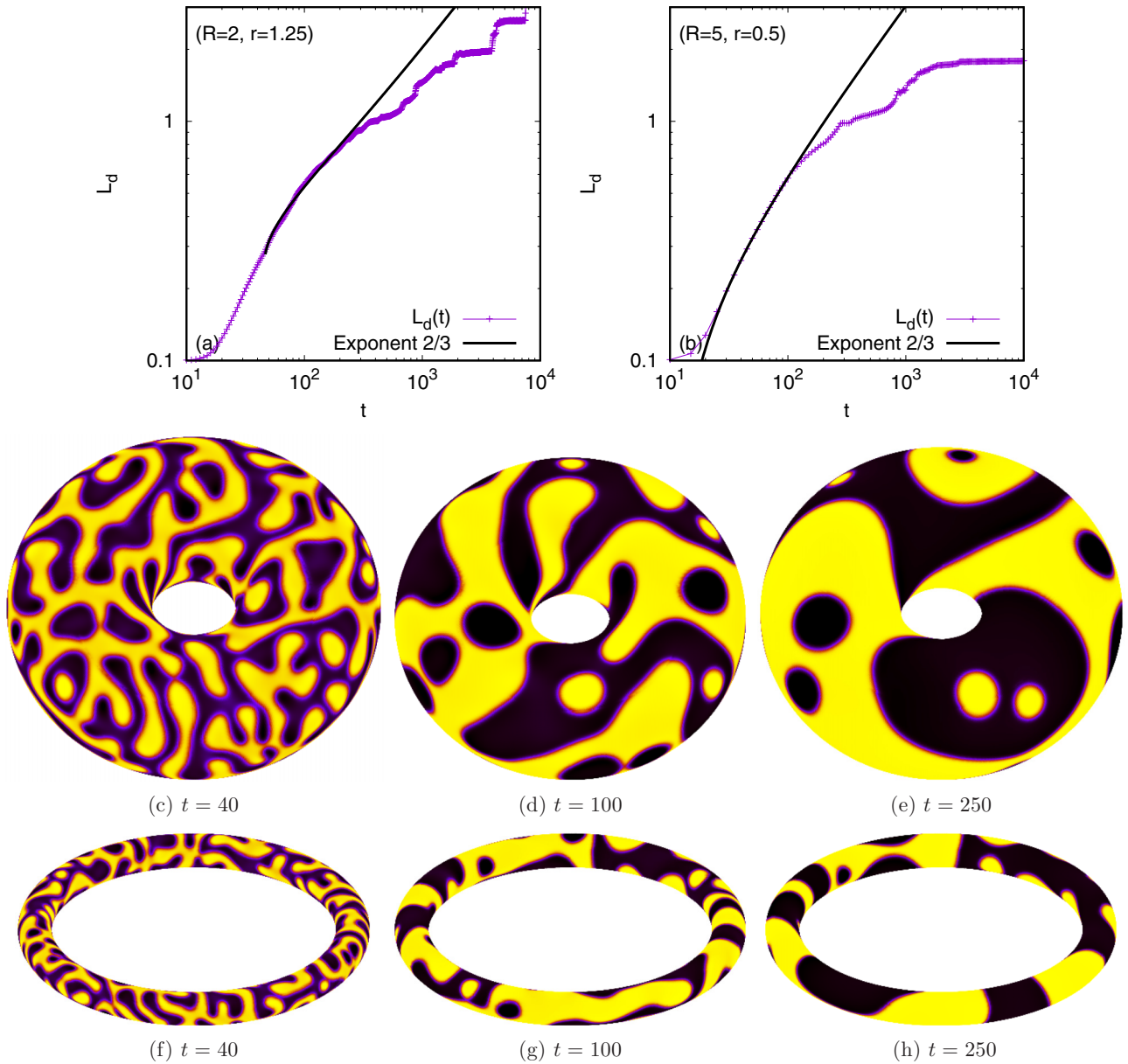
FIG. 11. Growth of the fluid domain size $L_d(t)$ for an even mixture on (a) a thick torus ($R = 2$, $r = 1.25$) and (b) a thin torus ($R = 5$, $r = 0.5$). (c)–(e) and (f)–(h) Snapshots of the typical fluid configurations at $t = 40$, 100, and 250 corresponding to the cases indicated in (a) and (b), respectively.

of hydrodynamics decreases as a function of the asymmetry of the mixture, though we do not yet know of a convincing systematic study of this effect. For example, Wagner and Cates [69] showed that at high concentrations droplets with hydrodynamics exhibit the viscous hydrodynamic coarsening regime, but as droplet coalescence is reduced at lower volume fractions the effect of hydrodynamics diminishes. Here, we observe the limit where the scaling is typical of that for diffusive dynamics.

The fluid configurations at various times in the simulation are shown in Figs. 12(b)–12(e), when hydrodynamics is taken into account. These can be compared to Figs. 12(f)–12(i), when the advection term is switched off in the Cahn-Hilliard equation. The differences are mainly that the morphologies with hydrodynamics are coarsening faster. In the

nonhydrodynamic simulation there are more coalescence events visible because the restoration of a round shape takes more time. Thus, while the scaling exponent is the same with and without hydrodynamics, hydrodynamics still plays an important role in that it allows coalescing droplets to return to a round shape more quickly.

### 2. Torus geometry

Here, we consider a torus geometry with $R = 2.5$ and $r = 1$ (same geometry and simulation parameters as in Fig. 10), and the order parameter is initialized according to Eq. (4.1) with $\bar{\phi} = -0.3$. The simulation results for the uneven mixture are shown in Fig. 13. Quantitatively, we find a similar behavior as for the Cartesian case. Both when hydrodynamics is
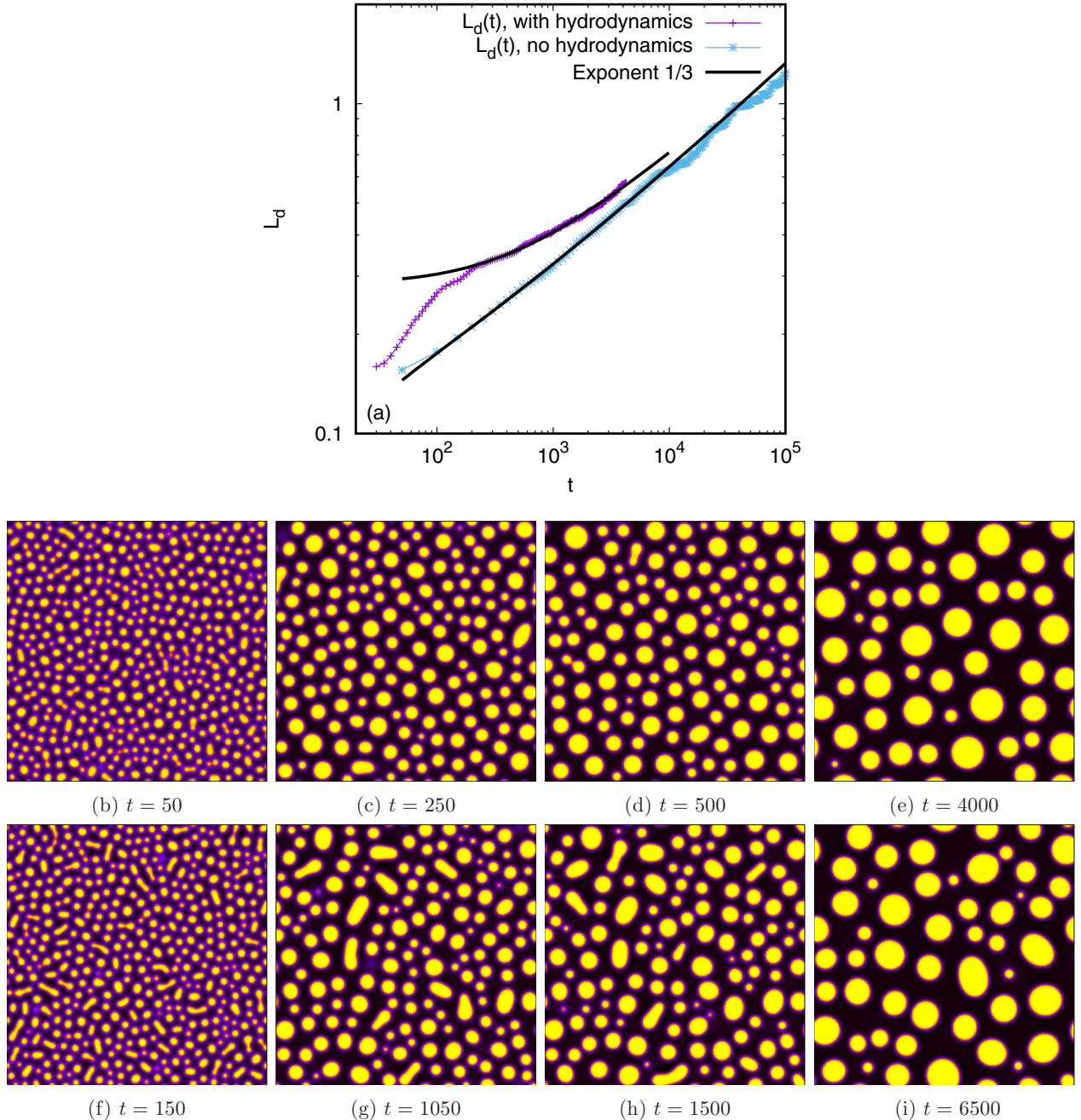
FIG. 12. (a) Growth of the fluid domain $L_d(t)$ for an uneven mixture ($\overline{\phi} = -0.3$) in two dimensions with and without hydrodynamics. In both cases, an exponent of $\frac{1}{3}$ characteristic of the diffusive regime is observed at late times. (b)–(e) Snapshots of the typical fluid configurations at times $t = 50, 250, 500$, and $4000$, corresponding to the case with hydrodynamics. (g)–(j) Snapshots of the fluid configurations corresponding to the case without hydrodynamics, at times $t = 150, 1050, 1500$, and $6500$. These are selected such that the values of $L_d(t)$ correspond to those in (b)–(e).

turned on and off, we observe a $\frac{1}{3}$ exponent in our simulations. Similar to the even mixture shown in Fig. 10, we also find that finite size effects occur earlier (smaller $L_d$) for the torus compared to the Cartesian geometry. As discussed in the case of even mixtures, this occurs when the fluid domains start to wrap around the circle in the poloidal direction. Snapshots of the fluid configurations during phase separation are shown in Figs. 13(b)–13(d) and 13(e)–13(g), respectively, for simulations with and without hydrodynamics.

At late times, the effect of the curvature on the domain dynamics becomes important. In Sec. III D we discussed how droplet domains migrate to the outer side of the torus. To quantify this effect during phase separation of uneven mixtures, we consider the average of $\phi$ with respect to the azimuthal angle $\varphi$:

$$\langle \phi \rangle = \int_0^{2\pi} \frac{d\varphi}{2\pi} \phi(\theta, \varphi). \tag{4.3}$$
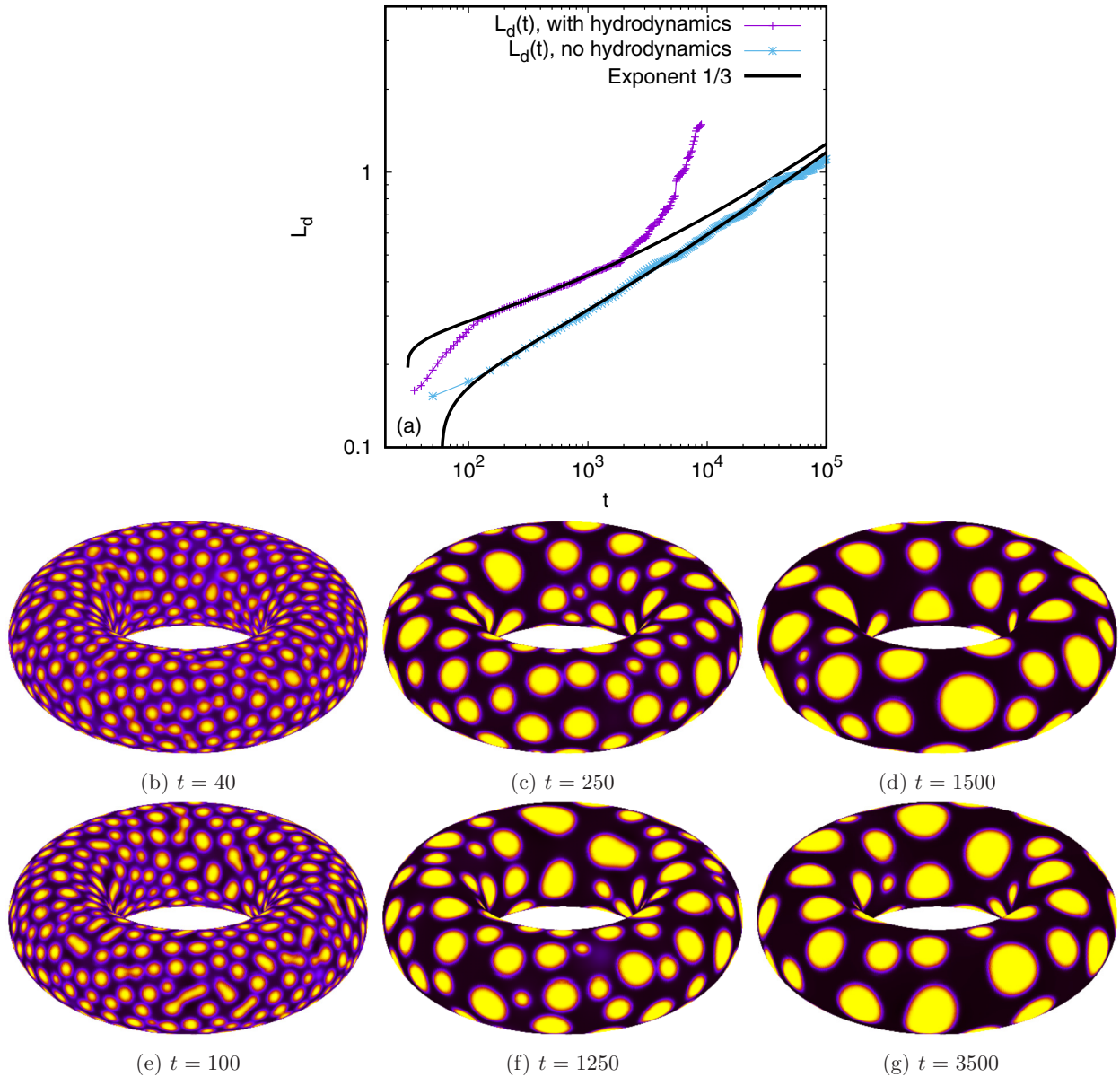
FIG. 13. (a) Growth of the fluid domain size $L_d(t)$ for an uneven mixture on a torus with $R = 2.5$ and $r = 1$ with and without hydrodynamics. (b)–(d) Snapshots of the typical fluid configurations at $t = 40$, 250, and 1500 corresponding to the case with hydrodynamics. (e)–(g) Snapshots of the typical fluid configurations at $t = 100$, 1250, and 3500 corresponding to the case without hydrodynamics. The times are chosen such that the values of $L_d$ match those in (b)–(d).

The discrete equivalent of the above relation is

$$\langle \phi \rangle_q = \frac{1}{N_\varphi} \sum_{s=1}^{N_\varphi} \phi_{s,q}. \tag{4.4}$$

We plot $(\langle \phi \rangle + 1)/2$ as a function of the poloidal angle $\theta$ at various times in Fig. 14(a). At late times [see, e.g., Fig. 14(c)], the typical configuration corresponds to the majority phase ($\phi = -1$) forming a continuum with several large droplets of the minority phase ($\phi = +1$) primarily in the outer side of the torus. At $t = 18\,000$ [Fig. 14(d)], when the steady state is reached, the inner stripe spans $0.65\pi \lesssim \theta \lesssim 1.35\pi$. The maximum of $(\langle \phi \rangle + 1)/2$ is clearly reached at $\theta = 0$, indicating that the outer side of the torus is populated by droplets centered on $\theta = 0$.

## V. CONCLUSIONS

In this work we developed a vielbein lattice Boltzmann scheme to solve the hydrodynamics equations of motion of a binary fluid on an arbitrary curved surface. To illustrate the application of our vielbein lattice Boltzmann method to curved surfaces, here we focused on the torus geometry and studied two classes of problems. First, due to the nonuniform curvature present on a torus, we showed drift motions of fluid droplets and stripes on a torus. Such dynamics are not present on a flat surface or on surfaces with uniform curvature. Interestingly, the fluid droplets and stripes display preference to different regions of the torus. Fluid droplets migrate to the outer side of the torus, while fluid stripes move to the inner side of the torus. The exhibited dynamics
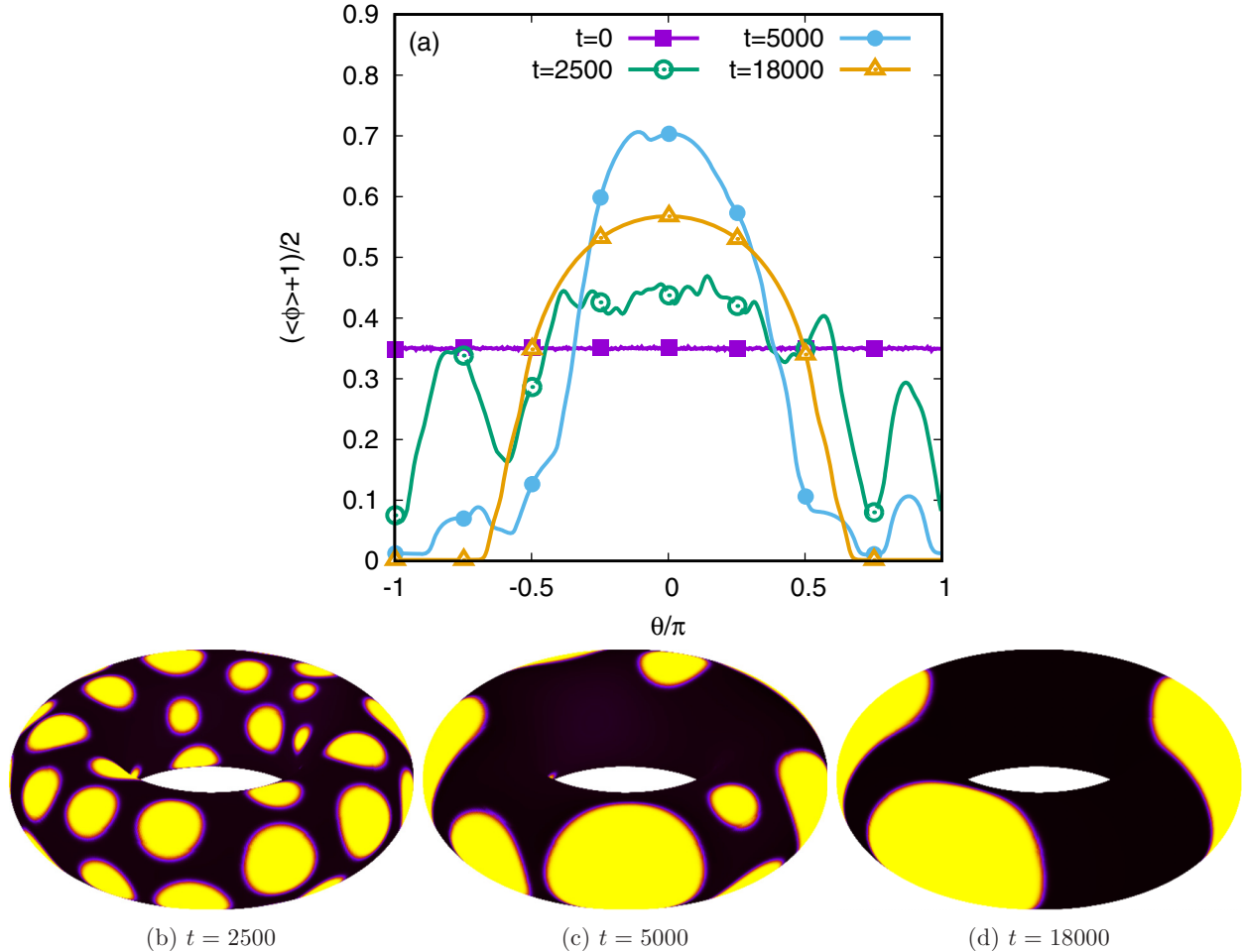
(b) $t = 2500$     (c) $t = 5000$     (d) $t = 18000$

FIG. 14. (a) The average distribution of the component $(\langle\phi\rangle + 1)/2$ as a function of $\theta$ at various times. (b)–(d) Snapshots of the fluid configurations at $t = 2500$, 5000, and 18 000.

is typical of a damped oscillatory motion. Moreover, for the fluid stripes, the corresponding dynamics can effectively be reduced to a one-dimensional problem by taking advantage of the symmetry with respect to the azimuthal angle. Our simulation results are in excellent agreement with the analytical predictions for the equilibrium position of the stripes, the Laplace pressure difference between the inside and outside of the stripes, and the relaxation dynamics of the stripes toward equilibrium.

We also studied phase separation dynamics on tori of various shapes. For even mixtures, $\frac{2}{3}$ and $\frac{1}{3}$ scaling exponents characteristic of hydrodynamics and diffusive regimes are observed. In contrast, for uneven mixtures, we only observe a $\frac{1}{3}$ scaling exponent both when hydrodynamics is turned on and off. Compared to Cartesian geometry, we saw that finite size effects kick in earlier for the torus geometry. By comparing the results for three torus aspect ratios, our observation seems to suggest that the perimeter in the poloidal direction is a key length scale for the appearance of finite size effects, corresponding to fluid domains wrapping around the circle in the poloidal direction. That the stripes are observed to form in the poloidal rather than the toroidal direction prevents the observation of drift motion of fluid stripes toward the inner side of the torus during phase separation. However, the

domain drifts for fluid drops to the outer side of the torus can be clearly observed at the late stage of phase separation.

While we focused on the torus geometry, our approach can be applied to arbitrary curved geometry. Moreover, one interesting area for future work is to expand the method to account for unstructured mesh, where the geometrical objects needed for the Boltzmann equation must be evaluated numerically. A major challenge is to construct a numerical scheme which is accurate to second order or higher. Another important avenue for future investigations is to couple the hydrodynamics equations of motion with more complex dynamical equations, such as those for (active and passive) liquid crystals and viscoelastic fluids. We believe this work extends the applicability of the lattice Boltzmann approaches to a new class of problems, complex flows on curved manifolds, which are difficult to carry out using the standard lattice Boltzmann method.

## APPENDIX A: APPLICATION OF THE VIELBEIN METHOD TO THE TORUS GEOMETRY

The derivation of the Boltzmann equation (2.16), written in conservative form with respect to vielbein vector fields, is discussed in [58]. Using Eq. (2.16) as a starting point, here we present generic main steps required to write the Boltzmann equation for any arbitrary curved surface. For concreteness, we focus on the torus geometry in this paper.

(1) *Parametrizing the surface.* As a two-dimensional manifold, a surface needs two coordinates $q^1$ and $q^2$ to be parametrized. In the case of a torus of inner radius $r$ and outer radius $R$, the parametrization can be chosen in terms of the angles $q^1 = \varphi \in [0, 2\pi)$ and $q^2 = \theta \in [0, 2\pi)$ as follows:

$$x = (R + r \cos\theta) \cos\varphi,$$
$$y = (R + r \cos\theta) \sin\varphi,$$
$$z = r \sin\theta, \qquad \text{(A1)}$$

and the system is periodic with respect to both of these angles.

(2) *Writing the line element.* Differentiating the functions $x$, $y$, and $z$ with respect to $q^1$ and $q^2$ yields the formula

$$ds^2 = g_{ab} dq^a dq^b, \quad g_{ab} = \delta_{ij} \frac{\partial x^i}{\partial q^a} \frac{\partial x^j}{\partial q^b}, \qquad \text{(A2)}$$

where $\{i, j\} \in \{1, 2, 3\}$, $1 \leqslant a, b \leqslant 2$, and $g_{ab}$ are the components of the metric tensor. In the case of Eq. (A1), the line element becomes

$$ds^2 = [dx^2 + dy^2 + dz^2]_{\text{on torus}}$$
$$= (R + r \cos\theta)^2 d\varphi^2 + r^2 d\theta^2, \qquad \text{(A3)}$$

leading to the metric tensor components

$$g_{\varphi\varphi} = (R + r \cos\theta)^2, \quad g_{\varphi\theta} = 0,$$
$$g_{\theta\theta} = r^2, \quad g_{\theta\varphi} = 0. \qquad \text{(A4)}$$

(3) *Constructing the vielbein field.* The vielbein vector frame consists of the vectors $\boldsymbol{e}_{\hat{a}} = e^a_{\hat{a}} \boldsymbol{\partial_a}$ which satisfy

$$g_{ab} e^a_{\hat{a}} e^b_{\hat{b}} = \delta_{\hat{a}\hat{b}}. \qquad \text{(A5)}$$

Since Eq. (A5) is invariant under the action of the orthogonal group with respect to the hatted indices, the vielbein is defined up to an arbitrary rotation. After fixing the vielbein, the vielbein one-form coframe denoted via $\boldsymbol{\omega}^{\hat{a}} = \omega^{\hat{a}}_a \boldsymbol{dq^a}$ is uniquely fixed by Eq. (2.3).

For the torus geometry, the natural choice is to take

$$\omega^{\hat{\varphi}}_\varphi = (R + r \cos\theta), \quad \omega^{\hat{\theta}}_\theta = r,$$
$$e^\varphi_{\hat{\varphi}} = \frac{1}{R + r \cos\theta}, \quad e^\theta_{\hat{\theta}} = \frac{1}{r}, \qquad \text{(A6)}$$

while $\omega^{\hat{\varphi}}_\theta = \omega^{\hat{\theta}}_\varphi = 0$ and $e^\theta_{\hat{\varphi}} = e^\varphi_{\hat{\theta}} = 0$.

(4) *Computing the Cartan coefficients.* The commutator of two vector fields $\boldsymbol{u}$ and $\boldsymbol{v}$ is another vector field, denoted by $[\boldsymbol{u}, \boldsymbol{v}] = (u^a \partial_a v^b - v^a \partial_a u^b) \boldsymbol{\partial_b}$. The contraction between the coframe one-form $\boldsymbol{\omega}^{\hat{c}}$ and the commutator of the tetrad frame vector fields $\boldsymbol{e}_{\hat{a}}$ and $\boldsymbol{e}_{\hat{b}}$ defines the Cartan coefficient $c_{\hat{a}\hat{b}}{}^{\hat{c}}$ (2.7), via the following relation:

$$c_{\hat{a}\hat{b}}{}^{\hat{c}} = \omega^{\hat{c}}_c \left( e^a_{\hat{a}} \partial_a e^c_{\hat{b}} - e^b_{\hat{b}} \partial_b e^c_{\hat{a}} \right). \qquad \text{(A7)}$$

In the case of the torus, the commutator of the vielbein vectors $\boldsymbol{e}_{\hat{\theta}}$ and $\boldsymbol{e}_{\hat{\varphi}}$ is

$$[\boldsymbol{e}_{\hat{\theta}}, \boldsymbol{e}_{\hat{\varphi}}] = -[\boldsymbol{e}_{\hat{\varphi}}, \boldsymbol{e}_{\hat{\theta}}] = \frac{\sin\theta}{R + r \cos\theta} \boldsymbol{e}_{\hat{\varphi}}, \qquad \text{(A8)}$$

leading to the Cartan coefficients

$$c_{\hat{\theta}\hat{\varphi}}{}^{\hat{\varphi}} = -c_{\hat{\varphi}\hat{\theta}}{}^{\hat{\varphi}} = \frac{\sin\theta}{R + r \cos\theta}. \qquad \text{(A9)}$$

(5) *Computing the connection coefficients.* In this paper, we employ the convention $\nabla_{\hat{b}} e_{\hat{a}} = \Gamma^{\hat{c}}{}_{\hat{a}\hat{b}} e_{\hat{c}}$ for the definition of the connection coefficients $\Gamma^{\hat{c}}{}_{\hat{a}\hat{b}}$, such that the covariant derivative of a vector is $\nabla_{\hat{a}} u^{\hat{b}} = e^c_{\hat{a}} \partial_c u^{\hat{b}} + \Gamma^{\hat{b}}{}_{\hat{c}\hat{a}} u^{\hat{c}}$. The connection coefficients can be computed using the Cartan coefficients as follows:

$$\Gamma^{\hat{c}}{}_{\hat{a}\hat{b}} = \tfrac{1}{2} \delta^{\hat{c}\hat{d}} (c_{\hat{d}\hat{a}\hat{b}} + c_{\hat{d}\hat{b}\hat{a}} - c_{\hat{a}\hat{b}\hat{d}}). \qquad \text{(A10)}$$

In the case of the torus, the only nonvanishing connection coefficients are

$$\Gamma^{\hat{\theta}}{}_{\hat{\varphi}\hat{\varphi}} = -\Gamma^{\hat{\varphi}}{}_{\hat{\theta}\hat{\varphi}} = \frac{\sin\theta}{R + r \cos\theta}. \qquad \text{(A11)}$$

(6) *Writing the Boltzmann equation.* Plugging Eq. (A11) into Eq. (2.16) yields the Boltzmann equation for the torus geometry, Eq. (2.17).

## APPENDIX B: VIELBEIN LATTICE BOLTZMANN ALGORITHM

The implementation of the lattice Boltzmann algorithm requires several ingredients. The first ingredient is the discretization of the velocity space. In this paper, we employ the Gauss-Hermite quadrature prescription and discretize the velocity space on each axis separately. We use Hermite polynomials obeying the following orthogonality relation:

$$\int_{-\infty}^{\infty} dx\, \omega(x) H_\ell(x) H_{\ell'}(x) = \ell!\, \delta_{\ell,\ell'}, \quad \omega(x) = \frac{e^{-x^2/2}}{\sqrt{2\pi}}. \quad \text{(B1)}$$

More properties of these polynomials relevant in the context of the LB method are given, e.g., in the Appendix of Ref. [70]. The Cartesian components $v_{k_\alpha}$ of the elements of the discrete velocity set along axis $\alpha$ are then equal to the roots of the Hermite polynomial $H_Q(v_{k_\alpha})$ ($1 \leqslant k_\alpha \leqslant Q$). Their values for $Q = 3$ and 4 are given in Eqs. (B19) and (B24), respectively. The resulting velocity set comprises $Q^2$ elements
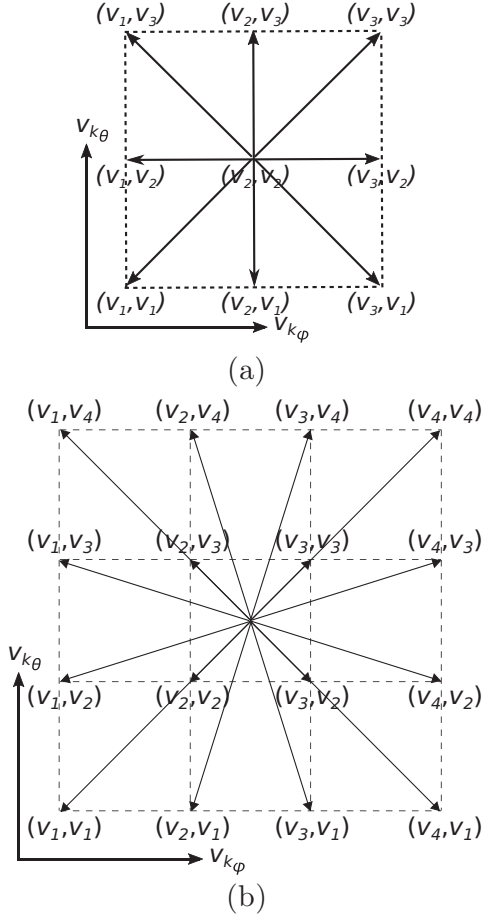
FIG. 15. The discrete velocity set employed by the lattice Boltzmann models based on the third (a) and fourth (b) order Gauss-Hermite quadratures. The filled black circle in the center of the figure corresponds to a lattice point in space. In our off-lattice implementation, the velocity directions do not coincide with neighboring lattice points.

$\boldsymbol{v_k} \equiv (v_{k_1}, v_{k_2})$, where $\boldsymbol{k} = (k_1, k_2)$ and $1 \leqslant k_1, k_2 \leqslant Q$. The cases $Q = 3$ and $4$ are illustrated in Figs. 15(a) and 15(b), respectively.

Following the discretization of the velocity space, the moments of $f$ and $f^{\mathrm{eq}}$ are replaced by quadrature sums. Introducing

$$\begin{pmatrix} \mathcal{M}^{(\ell)}_{\alpha_1 \ldots \alpha_\ell} \\ \mathcal{M}^{\mathrm{eq};(\ell)}_{\alpha_1 \ldots \alpha_\ell} \end{pmatrix} \equiv \int d\boldsymbol{v} \begin{pmatrix} f \\ f^{\mathrm{eq}} \end{pmatrix} v_{\alpha_1} \ldots v_{\alpha_\ell}, \qquad (\text{B2})$$

where $d\boldsymbol{v} = dv^{\hat{1}} dv^{\hat{2}}$ is the integration measure on the two-dimensional velocity space, the Gauss-Hermite quadrature rule recovers the velocity space integration via

$$\begin{pmatrix} \mathcal{M}^{Q;(\ell)}_{\alpha_1 \ldots \alpha_\ell} \\ \mathcal{M}^{\mathrm{eq};Q;(\ell)}_{\alpha_1 \ldots \alpha_\ell} \end{pmatrix} = \sum_{\boldsymbol{k}} \begin{pmatrix} f_{\boldsymbol{k}} \\ f^{\mathrm{eq}}_{\boldsymbol{k}} \end{pmatrix} v_{k_{\alpha_1}} \ldots v_{k_{\alpha_\ell}}. \qquad (\text{B3})$$

The connection between the discrete populations $f_{\boldsymbol{k}}$ and the Boltzmann distribution $f$ is made through

$$f_{\boldsymbol{k}} = \frac{w_{\boldsymbol{k}}}{\omega(\boldsymbol{v_k})} f(\boldsymbol{v_k}), \qquad \omega(\boldsymbol{v}) = \frac{e^{-\boldsymbol{v}^2/2}}{2\pi}. \qquad (\text{B4})$$

A similar relation can be written for $f^{\mathrm{eq}}_{\boldsymbol{k}}$. The quadrature weights $w_{\boldsymbol{k}} \equiv w_{k_1} w_{k_2}$ appearing above are obtained as the product of the one-dimensional Gauss-Hermite quadrature weights, which are computed using the following formula [71]:

$$w_k = \frac{Q!}{H^2_{Q+1}(v_k)}. \qquad (\text{B5})$$

The weights corresponding to the particular cases $Q = 3$ and $4$ are given in Eqs. (B20) and (B25), respectively.

The second ingredient concerns the BGK collision term. We first consider an expansion of $f^{\mathrm{eq}}$ with respect to the tensorial Hermite polynomials [72]:

$$f^{\mathrm{eq}} = n\omega(\boldsymbol{v}) \sum_{\ell=0}^{\infty} \frac{1}{\ell!} \mathcal{H}^{(\ell)}_{\alpha_1 \ldots \alpha_\ell}(\boldsymbol{v_k}) a^{\mathrm{eq};(\ell)}_{\alpha_1 \ldots \alpha_\ell}. \qquad (\text{B6})$$

The first few tensorial Hermite polynomials are reproduced below:

$$\mathcal{H}^{(0)}(\boldsymbol{v}) = 1, \quad \mathcal{H}^{(1)}_\alpha(\boldsymbol{v}) = v_\alpha, \quad \mathcal{H}^{(2)}_{\alpha\beta}(\boldsymbol{v}) = v_\alpha v_\beta - \delta_{\alpha\beta},$$

$$\mathcal{H}^{(3)}_{\alpha\beta\gamma}(\boldsymbol{v}) = v_\alpha v_\beta v_\gamma - (v_\alpha \delta_{\beta\gamma} + v_\beta \delta_{\alpha\gamma} + v_\gamma \delta_{\alpha\beta}). \qquad (\text{B7})$$

The expansion coefficients $a^{\mathrm{eq};(\ell)}_{\alpha_1 \ldots \alpha_\ell}$ appearing in Eq. (B10) are obtained with the help of the orthogonality relation of the tensorial Hermite polynomials:

$$a^{\mathrm{eq};(\ell)}_{\alpha_1 \ldots \alpha_\ell} = \int d\boldsymbol{v} \, f^{\mathrm{eq}} \mathcal{H}^{(\ell)}_{\alpha_1 \ldots \alpha_\ell}(\boldsymbol{v}). \qquad (\text{B8})$$

In particular, the first few coefficients for the case of an isothermal flow at temperature $T = 1$ are [72]

$$a^{\mathrm{eq};(0)} = n, \quad a^{\mathrm{eq};(1)}_\alpha = nu_\alpha, \quad a^{\mathrm{eq};(2)}_{\alpha\beta} = nu_\alpha u_\beta,$$

$$a^{\mathrm{eq};(3)}_{\alpha\beta\gamma} = nu_\alpha u_\beta u_\gamma. \qquad (\text{B9})$$

In order to preserve the collision invariants $\psi \in \{1, \boldsymbol{v}\}$ of the BGK model after the discretization of the velocity space, the expansion of $f^{\mathrm{eq}}$ in Eq. (B6) must be truncated at order $N = Q - 1$:

$$f^{Q;\mathrm{eq}}_{\boldsymbol{k}} = nw_{\boldsymbol{k}} \sum_{\ell=0}^{Q-1} \frac{1}{\ell!} \mathcal{H}^{(\ell)}_{\alpha_1 \ldots \alpha_\ell}(\boldsymbol{v_k}) a^{\mathrm{eq};(\ell)}_{\alpha_1 \ldots \alpha_\ell}. \qquad (\text{B10})$$

The superscript $Q$ of $f^{Q;\mathrm{eq}}_{\boldsymbol{k}}$ indicates that only terms up to $Q - 1$ are included in the expansion. The expressions of $f^{Q;\mathrm{eq}}_{\boldsymbol{k}}$ employed for $Q = 3$ and $4$ are given in Eqs. (B21) and (B26), respectively.

The third ingredient refers to the computation of the force terms. In order to preserve consistency with the procedure for the velocity space discretization, we consider a unidimensional expansion of the distribution function $f$ with respect to the velocity space degrees of freedom (for definiteness, we focus on the axis $\alpha = 1$) in terms of the Hermite polynomials [58,73]:

$$f = \omega(v_1) \sum_{\ell_1=0}^{\infty} \frac{1}{\ell_1!} \mathcal{F}^1_{\ell_1}(v_2) H_{\ell_1}(v_1). \qquad (\text{B11})$$

A similar expansion can be written with respect to $v_2$, essentially by performing the swap $1 \leftrightarrow 2$. The expansion

coefficients $\mathcal{F}^1_{\ell_1}(v_2)$ are obtained using the orthogonality property in Eq. (B1):

$$\mathcal{F}^1_{\ell_1}(v_2) = \int_{-\infty}^{\infty} dv_1 \, f(v_1, v_2) H_{\ell_1}(v_1). \tag{B12}$$

We now consider similar expansions of the velocity space derivatives of $f$ which are relevant in the context of this paper:

$$\frac{\partial f}{\partial v_1} = \omega(v_1) \sum_{\ell_1=0}^{\infty} \frac{1}{\ell_1!} \mathcal{F}^{1'}_{\ell_1}(v_2) H_{\ell_1}(v_1),$$

$$\frac{\partial(f v_1)}{\partial v_1} = \omega(v_1) \sum_{\ell_1=0}^{\infty} \frac{1}{\ell_1!} \widetilde{\mathcal{F}}^{1'}_{\ell_1}(v_2) H_{\ell_1}(v_1). \tag{B13}$$

An integration by parts shows that the expansion coefficients $\mathcal{F}^{1'}_{\ell_1}(v_2)$ and $\widetilde{\mathcal{F}}^{1'}_{\ell_1}(v_2)$ can be related to $\mathcal{F}^1_{\ell_1}(v_2)$ through

$$\mathcal{F}^{1'}_{\ell_1}(v_2) = -\ell_1 \mathcal{F}^1_{\ell_1-1}(v_2),$$

$$\widetilde{\mathcal{F}}^{1'}_{\ell_1}(v_2) = -\ell_1 \big[ \mathcal{F}^1_{\ell_1}(v_2) + (\ell_1 - 1) \mathcal{F}^1_{\ell_1-2}(v_2) \big]. \tag{B14}$$

After the discretization of the velocity space, the expansion coefficients $\mathcal{F}^1_{\ell_1}(v_2)$ are obtained from $f_{\boldsymbol{k}}$ through

$$\mathcal{F}^1_{\ell_1;k_2} = \sum_{k_1=1}^{Q} f_{\boldsymbol{k}} H_{\ell_1}(v_{k_1}), \tag{B15}$$

such that Eq. (B14) becomes

$$\mathcal{F}^{1'}_{\ell_1;k_2} = -\ell_1 \sum_{k_1=1}^{Q} f_{\boldsymbol{k}} H_{\ell_1-1}(v_{k_1}),$$

$$\widetilde{\mathcal{F}}^{1'}_{\ell_1;k_2} = -\ell_1 \sum_{k_1=1}^{Q} f_{\boldsymbol{k}} \big[ H_{\ell_1}(v_{k_1}) + (\ell_1 - 1) H_{\ell_1-2}(v_{k_1}) \big]. \tag{B16}$$

Substituting Eq. (B16) into Eq. (B13), it can be seen that $\partial f/\partial v_1$ and $\partial(f v_1)/\partial v_1$ are linear with respect to $f$. After discretization, Eq. (B13) can be written as

$$\left( \frac{\partial f}{\partial v_1} \right)_{\boldsymbol{k}} = \sum_{k'_1=1}^{Q} \mathcal{K}^H_{k_1,k'_1} f_{k'_1,k_2},$$

$$\left( \frac{\partial(f v_1)}{\partial v_1} \right)_{\boldsymbol{k}} = \sum_{k'_1=1}^{Q} \widetilde{\mathcal{K}}^H_{k_1,k'_1} f_{k'_1,k_2}. \tag{B17}$$

The kernels $\mathcal{K}^H_{k,k'}$ and $\widetilde{\mathcal{K}}^H_{k,k'}$ can be written in terms of the Hermite polynomials, as follows [58]:

$$\mathcal{K}^H_{k,k'} = -w_k \sum_{\ell=0}^{Q-1} \frac{1}{\ell!} H_{\ell+1}(v_k) H_{\ell}(v_{k'}),$$

$$\widetilde{\mathcal{K}}^H_{k,k'} = -w_k \sum_{\ell=0}^{Q-1} \frac{1}{\ell!} H_{\ell+1}(v_k) [H_{\ell+1}(v_{k'}) + \ell H_{\ell-1}(v_{k'})], \tag{B18}$$

where the summation ends at $Q-1$ since $H_Q(v_k) = H_Q(v_{k'}) = 0$. The exact expressions for the kernels introduced above are given separately for the cases $Q = 3$ and 4 in Appendices B 1 and B 2, respectively.

The fourth and final ingredient concerns the streaming step. In this paper, we employ finite difference schemes to deal with this step. Further details are summarized in Appendix C.

### 1. $Q = 3$ implementation

The nine velocity directions, corresponding to $Q = 3$, are illustrated in Fig. 15(a). The possible values of $v_{k_1}$ and $v_{k_2}$ ($1 \leqslant k_1, \ k_2 \leqslant 3$) are given as the roots of the third order Hermite polynomial $H_3(x) = x^3 - 3x$. Specifically, we employ

$$\begin{pmatrix} v_1 \\ v_2 \\ v_3 \end{pmatrix} = \begin{pmatrix} -\sqrt{3} \\ 0 \\ \sqrt{3} \end{pmatrix}. \tag{B19}$$

The quadrature weights computed using Eq. (B5) [we use $H_4(x) = x^4 - 6x^2 + 3$] are

$$w_1 = w_3 = \tfrac{1}{6}, \quad w_2 = \tfrac{2}{3}. \tag{B20}$$

The Maxwell-Boltzmann distribution corresponding to $Q = 3$ can be obtained from Eq. (B10):

$$f_{\boldsymbol{k}}^{Q=3;\text{eq}} = n w_{\boldsymbol{k}} \big\{ 1 + \boldsymbol{v_k} \cdot \boldsymbol{u} + \tfrac{1}{2} [(\boldsymbol{v_k} \cdot \boldsymbol{u})^2 - \boldsymbol{u}^2] \big\}. \tag{B21}$$

It is clear that the above expression cannot reproduce the third order moment $\mathcal{M}^{\text{eq};(3)}_{\alpha\beta\gamma}$. Indeed, using the ingredients above, we obtain

$$\mathcal{M}^{\text{eq};Q=3;(3)}_{\alpha\beta\gamma} = \mathcal{M}^{\text{eq};(3)}_{\alpha\beta\gamma} - n u_\alpha u_\beta u_\gamma. \tag{B22}$$

The above error term is third order with respect to the Mach number and is usually neglectable in the LB community.

Finally, the kernel matrices for the constructing the force terms, given in Eq. (B18), are

$$\mathcal{K}^H_{k,k'} = \begin{pmatrix} \frac{\sqrt{3}}{2} & \frac{1}{2\sqrt{3}} & -\frac{1}{2\sqrt{3}} \\ -\frac{2}{\sqrt{3}} & 0 & \frac{2}{\sqrt{3}} \\ \frac{1}{2\sqrt{3}} & -\frac{1}{2\sqrt{3}} & -\frac{\sqrt{3}}{2} \end{pmatrix},$$

$$\widetilde{\mathcal{K}}^H_{k,k'} = \begin{pmatrix} -\frac{3}{2} & 0 & -\frac{1}{2} \\ 2 & 0 & 2 \\ -\frac{1}{2} & 0 & -\frac{3}{2} \end{pmatrix}. \tag{B23}$$

After introducing the above kernels into Eq. (B17), it can be seen that the expansion coefficients $\mathcal{F}'_{\ell_1;k_2}$ and $\widetilde{\mathcal{F}}'_{\ell_1;k_2}$ can be retrieved exactly for $0 \leqslant \ell_1 \leqslant 2$, while $\mathcal{F}'_{3;k_2} = \widetilde{\mathcal{F}}'_{3;k_2} = 0$.

### 2. $Q = 4$ implementation

The velocity components $\{v_{k_\varphi}, v_{k_\theta}\}$ ($1 \leqslant k_\theta, \ k_\varphi \leqslant 4$) corresponding to $Q = 4$ are obtained as the roots of the fourth order Hermite polynomial $H_4(x) = x^4 - 6x^2 + 3$. Explicitly, their values are [70]

$$\begin{pmatrix} v_1 \\ v_2 \\ v_3 \\ v_4 \end{pmatrix} = \begin{pmatrix} -\sqrt{3 + \sqrt{6}} \\ -\sqrt{3 - \sqrt{6}} \\ \sqrt{3 - \sqrt{6}} \\ \sqrt{3 + \sqrt{6}} \end{pmatrix}. \tag{B24}$$

It is worth noting that, unlike the $Q = 3$ case, in general these velocity directions cannot be made to simultaneously coincide with the neighboring lattice points. The weights corresponding to $Q = 4$ can be obtained from Eq. (B5), by noting that $H_5(x) = x^5 - 10x^3 + 15x$:

$$w_1 = w_4 = \frac{3 - \sqrt{6}}{12}, \quad w_2 = w_3 = \frac{3 + \sqrt{6}}{12}. \quad \text{(B25)}$$

The discrete equilibrium populations $f_{\bm{k}}^{\text{eq}}$ can be obtained from Eq. (B10) [70,72]:

$$f_{\bm{k}}^{Q=4;\text{eq}} = n w_{k_\theta} w_{k_\varphi} \left\{ 1 + \bm{v_k} \cdot \bm{u} + \tfrac{1}{2}[(\bm{v_k} \cdot \bm{u})^2 - \bm{u}^2] \right.$$
$$\left. + \tfrac{1}{6}\bm{v_k} \cdot \bm{u}[(\bm{v_k} \cdot \bm{u})^2 - 3\bm{u}^2] \right\}. \quad \text{(B26)}$$

The kernels required for the computation of the force terms, introduced in Eq. (B18), have the following structure [74]:

$$\mathcal{K}_{i,m}^H = \begin{pmatrix} \frac{1}{2}\sqrt{3 + \sqrt{6}} & \frac{\sqrt{3+\sqrt{3}}}{2(3+\sqrt{6})} & -\frac{\sqrt{3-\sqrt{3}}}{2(3+\sqrt{6})} & \frac{1}{2}\sqrt{1 - \sqrt{\frac{2}{3}}} \\ -\sqrt{\frac{5+2\sqrt{6}}{2(3-\sqrt{3})}} & \frac{1}{2}\sqrt{3 - \sqrt{6}} & \frac{1}{2}\sqrt{1 + \sqrt{\frac{2}{3}}} & -\frac{\sqrt{27+11\sqrt{6}}-\sqrt{3+\sqrt{6}}}{2\sqrt{6}} \\ \frac{\sqrt{27+11\sqrt{6}}-\sqrt{3+\sqrt{6}}}{2\sqrt{6}} & -\frac{1}{2}\sqrt{1 + \sqrt{\frac{2}{3}}} & -\frac{1}{2}\sqrt{3 - \sqrt{6}} & \frac{\sqrt{27+11\sqrt{6}}+\sqrt{3+\sqrt{6}}}{2\sqrt{6}} \\ -\frac{\sqrt{3-\sqrt{6}}}{2\sqrt{3}} & \frac{\sqrt{3-\sqrt{3}}}{2(3+\sqrt{6})} & -\frac{\sqrt{3+\sqrt{3}}}{2(3+\sqrt{6})} & -\frac{1}{2}\sqrt{3 + \sqrt{6}} \end{pmatrix},$$

$$\widetilde{\mathcal{K}}_{i,m}^H = \begin{pmatrix} -\frac{3+\sqrt{6}}{2} & \frac{2-5\sqrt{2}+\sqrt{6(9-4\sqrt{2})}}{4} & \frac{2+5\sqrt{2}-\sqrt{6(9+4\sqrt{2})}}{4} & \frac{1}{2} \\ \frac{2+5\sqrt{2}+4\sqrt{3}+\sqrt{6}}{4} & -\frac{3-\sqrt{6}}{2} & \frac{1}{2} & \frac{2-5\sqrt{2}-4\sqrt{3}+\sqrt{6}}{4} \\ \frac{2-5\sqrt{2}-4\sqrt{3}+\sqrt{6}}{4} & \frac{1}{2} & -\frac{3-\sqrt{6}}{2} & \frac{2+5\sqrt{2}+4\sqrt{3}+\sqrt{6}}{4} \\ \frac{1}{2} & \frac{2+5\sqrt{2}-\sqrt{6(9+4\sqrt{2})}}{4} & \frac{2-5\sqrt{2}+\sqrt{6(9-4\sqrt{2})}}{4} & -\frac{3+\sqrt{6}}{2} \end{pmatrix}. \quad \text{(B27)}$$

### 3. Chapman-Enskog analysis

We now consider the recovery of the Navier-Stokes equations via the Chapman-Enskog expansion. We begin by discussing the familiar case of the Cartesian geometry, after which the torus geometry is considered.

In the so-called simplified version of the Chapman-Enskog method, the deviation from equilibrium $\delta f = f - f^{(\text{eq})}$ of the distribution function is considered to be of the same order of magnitude as the relaxation time $\tau$, which is regarded as a small quantity. Noting that $J[f] = -\delta f/\tau$ in the BGK model, at zeroth order, the distribution on the left hand side of the Boltzmann equation (2.16) can be replaced by $f^{(\text{eq})}$, allowing $\delta f$ to be obtained as

$$\delta f = -\tau \left\{ \frac{\partial f^{\text{eq}}}{\partial t} + \frac{1}{\sqrt{g}} \frac{\partial}{\partial q^b} (v^{\hat{a}} e_{\hat{a}}^b f^{\text{eq}} \sqrt{g}) \right.$$
$$\left. + \frac{\partial}{\partial v^{\hat{a}}} \left[ \left( \frac{F^{\hat{a}}}{m} - \Gamma^{\hat{a}}_{\hat{b}\hat{c}} v^{\hat{b}} v^{\hat{c}} \right) f^{\text{eq}} \right] \right\}. \quad \text{(B28)}$$

The viscous part $\sigma_{\hat{a}\hat{b}} = T_{\hat{a}\hat{b}} - P\delta_{\hat{a}\hat{b}}$ of the stress tensor can be obtained as a moment of $\delta f$:

$$\sigma_{\hat{a}\hat{b}} = m \int d\bm{v} \, \delta f \, \xi_{\hat{a}} \xi_{\hat{b}} = m \int d\bm{v} \, \delta f \, v_{\hat{a}} v_{\hat{b}}, \quad \text{(B29)}$$

where $\xi_{\hat{a}} = v_{\hat{a}} - u_{\hat{a}}$ is the peculiar velocity and the equality follows by noting that the preservation of the collision invariants $\psi \in \{1, v^{\hat{a}}\}$ of $J[f]$ entails

$$\int d\bm{v} \, \delta f = \int d\bm{v} \, \delta f \, v^{\hat{a}} = 0. \quad \text{(B30)}$$

Multiplying Eq. (B28) by $v_{\hat{a}} v_{\hat{b}}$ and integrating with respect to the velocity space shows that the recovery of $\sigma_{\hat{a}\hat{b}}$ requires various moments of the equilibrium distribution $f^{(\text{eq})}$ and its derivatives in the velocity space.

We first focus on the Cartesian geometry, in which case Eq. (B28) becomes

$$\delta f = -\tau \left( \frac{\partial f^{\text{eq}}}{\partial t} + \bm{v} \cdot \bm{\nabla} f^{\text{eq}} + \frac{\bm{F}}{m} \cdot \bm{\nabla}_{\bm{v}} f^{\text{eq}} \right). \quad \text{(B31)}$$

It can be seen that the correct recovery of $\sigma_{\hat{a}\hat{b}}$ is subject to the recovery of the third moment of $f^{\text{eq}}$. When $Q = 3$, the error highlighted in Eq. (B22) induces a deviation from $\sigma_{\hat{a}\hat{b}}$ as given in Eq. (2.20):

$$\sigma_{\hat{a}\hat{b}}^{Q=3} = \sigma_{\hat{a}\hat{b}} + \tau \bm{\nabla}^{\hat{c}} (\rho u_{\hat{a}} u_{\hat{b}} u_{\hat{c}}). \quad \text{(B32)}$$

Since this error is of third order with respect to the local Mach number, it is generally regarded as negligible. When $Q = 4$, no such error appears and $\sigma_{\hat{a}\hat{b}}$ is correctly recovered:

$$\sigma_{\hat{a}\hat{b}}^{Q=4} = \sigma_{\hat{a}\hat{b}}. \quad \text{(B33)}$$

In the case of the torus geometry, Eq. (B28) reduces to

$$\delta f = -\tau \left\{ \frac{\partial f^{(\text{eq})}}{\partial t} + \frac{v^{\hat{\varphi}}}{R(1 + a\cos\theta)} \frac{\partial f^{(\text{eq})}}{\partial \varphi} \right.$$
$$+ \frac{v^{\hat{\theta}}}{r(1 + a\cos\theta)} \frac{\partial[f^{(\text{eq})}(1 + a\cos\theta)]}{\partial\theta}$$
$$- \frac{\sin\theta}{R(1 + a\cos\theta)} \left[ v^{\hat{\varphi}} \frac{\partial(f^{(\text{eq})} v^{\hat{\varphi}})}{\partial v^{\hat{\theta}}} - v^{\hat{\theta}} \frac{\partial(f^{(\text{eq})} v^{\hat{\varphi}})}{\partial v^{\hat{\varphi}}} \right]$$
$$\left. + \frac{F^{\hat{\varphi}}}{m} \frac{\partial f^{(\text{eq})}}{\partial v^{\hat{\varphi}}} + \frac{F^{\hat{\theta}}}{m} \frac{\partial f^{(\text{eq})}}{\partial v^{\hat{\theta}}} \right\}. \quad \text{(B34)}$$

At $Q = 3$, aside from the error coming from the advection term, due to the inaccurate recovery of the third order moment
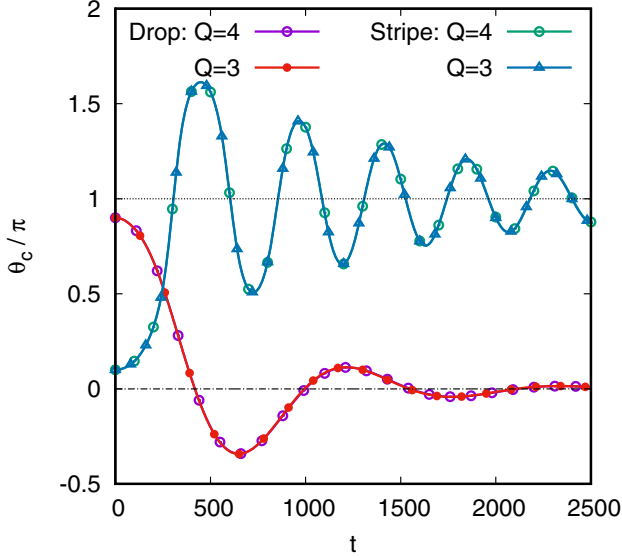
FIG. 16. Time evolution of the stripe and drop center $\theta_c$, for a stripe initialized at $\theta_0 = 0.1\pi$ and a drop initialized at $\theta_0 = 0.9\pi$, using both $Q = 3$ and 4 implementations. The results overlap for all times.

of $f^{\mathrm{eq}}$, there is another source of errors, coming from the inertial term. The errors introduced are always of order Ma$^3$ and contribute such that the relation in Eq. (B32) between the apparent viscous stress $\sigma_{\hat{a}\hat{b}}^{Q=3}$ and the physical one $\sigma_{\hat{a}\hat{b}}$ is exactly retained. For completeness, we give below the relevant moments of the inertial terms for which a deviation is seen at $Q = 3$:

$$\sum_{\boldsymbol{k}} v_{k_1}^3 v_{k_2} \left( \frac{\partial f^{\mathrm{eq}}}{\partial v_2} \right)_{\boldsymbol{k}} = \int d\boldsymbol{v} \, v_1^3 v_2 \frac{\partial f^{\mathrm{eq}}}{\partial v_2} + \rho u_1^3,$$

$$\sum_{\boldsymbol{k}} v_{k_1}^2 v_{k_2}^2 \left( \frac{\partial f^{\mathrm{eq}}}{\partial v_2} \right)_{\boldsymbol{k}} = \int d\boldsymbol{v} \, v_1^2 v_2^2 \frac{\partial f^{\mathrm{eq}}}{\partial v_2} + 2\rho u_1^2 u_2,$$

$$\sum_{\boldsymbol{k}} v_{k_1}^2 v_{k_2} \left[ \frac{\partial (f^{\mathrm{eq}} v_1)}{\partial v_1} \right]_{\boldsymbol{k}} = \int d\boldsymbol{v} \, v_1^2 v_2 \frac{\partial (f^{\mathrm{eq}} v_1)}{\partial v_1} + 2\rho u_1^2 u_2,$$

$$\sum_{\boldsymbol{k}} v_{k_1} v_{k_2}^2 \left[ \frac{\partial (f^{\mathrm{eq}} v_1)}{\partial v_1} \right]_{\boldsymbol{k}} = \int d\boldsymbol{v} \, v_1 v_2^2 \frac{\partial (f^{\mathrm{eq}} v_1)}{\partial v_1} + \rho u_1 u_2^2. \tag{B35}$$

As before, no errors are seen in the case when $Q = 4$.

#### 4. Convergence test

The previous subsection showed that a third order quadrature ($Q = 3$) introduces errors of order $O(\mathrm{Ma}^3)$ in the recovery of the Navier-Stokes equations. In order to assess the relevance of these errors, the simulations reported in the main body of the paper were performed using both $Q = 3$ and 4.

We begin this section by showing a comparison of the results for the fluid stripes and drops migration discussed in Secs. III A and III D, respectively. Since the deviations between $Q = 3$ and 4 are expected to be more significant at larger fluid velocities, we choose the initializations corresponding to the largest initial amplitude of the stripe
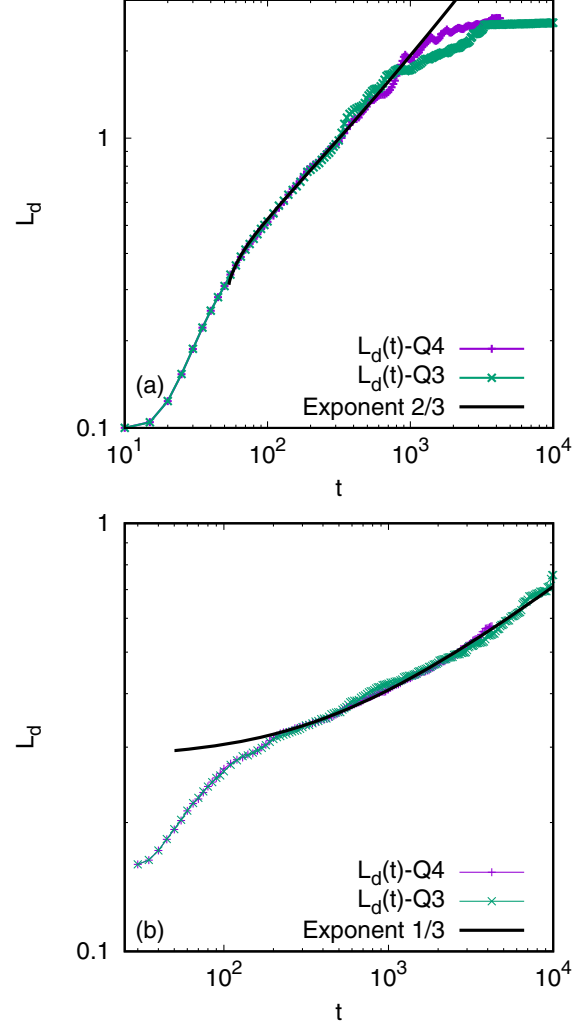


FIG. 17. Comparison of the growth of the fluid domain size $L_d(t)$ in the inertial-hydrodynamics regime in two dimensions for (a) an even mixture and (b) an uneven mixture, using the $Q = 3$ and 4 implementations. Minor discrepancies can be observed at late times.

($\theta_c = \pi/10$) and drop ($\theta_c = 9\pi/10$). The comparison can be seen in Fig. 16. The agreement is excellent, showing that the regime in which these phenomena occur is not affected by the spurious $O(\mathrm{Ma}^3)$ terms appearing in the Navier-Stokes equations at $Q = 3$.

We now consider the domain growth for the initial conditions considered in Sec. IV. Figure 17 shows $L_d(t)$ computed in the case of the Cartesian geometry, for the even [Fig. 17(a)] and uneven [Fig. 17(b)] initial compositions, as discussed in Sec. IV. The results corresponding to $Q = 4$, shown with purple lines and + symbols, are identical to those reported in Figs. 9(a) and 12(a). A small discrepancy between the $Q = 3$ and 4 results can be seen at late times, essentially at the time when the domain growth rate is affected by finite size effects. Similar discrepancies can be seen in Fig. 18, in the case of the torus geometry. The even and uneven initial compositions on the torus with $R = 2.5$ and $r = 1$ are shown in Figs. 18(a) and 18(b), where the $Q = 4$ results are identical to those reported in Figs. 10(a) and 13(a) (only the results with hydrodynamics are shown). Figures 18(c) and 18(d) show the results for even
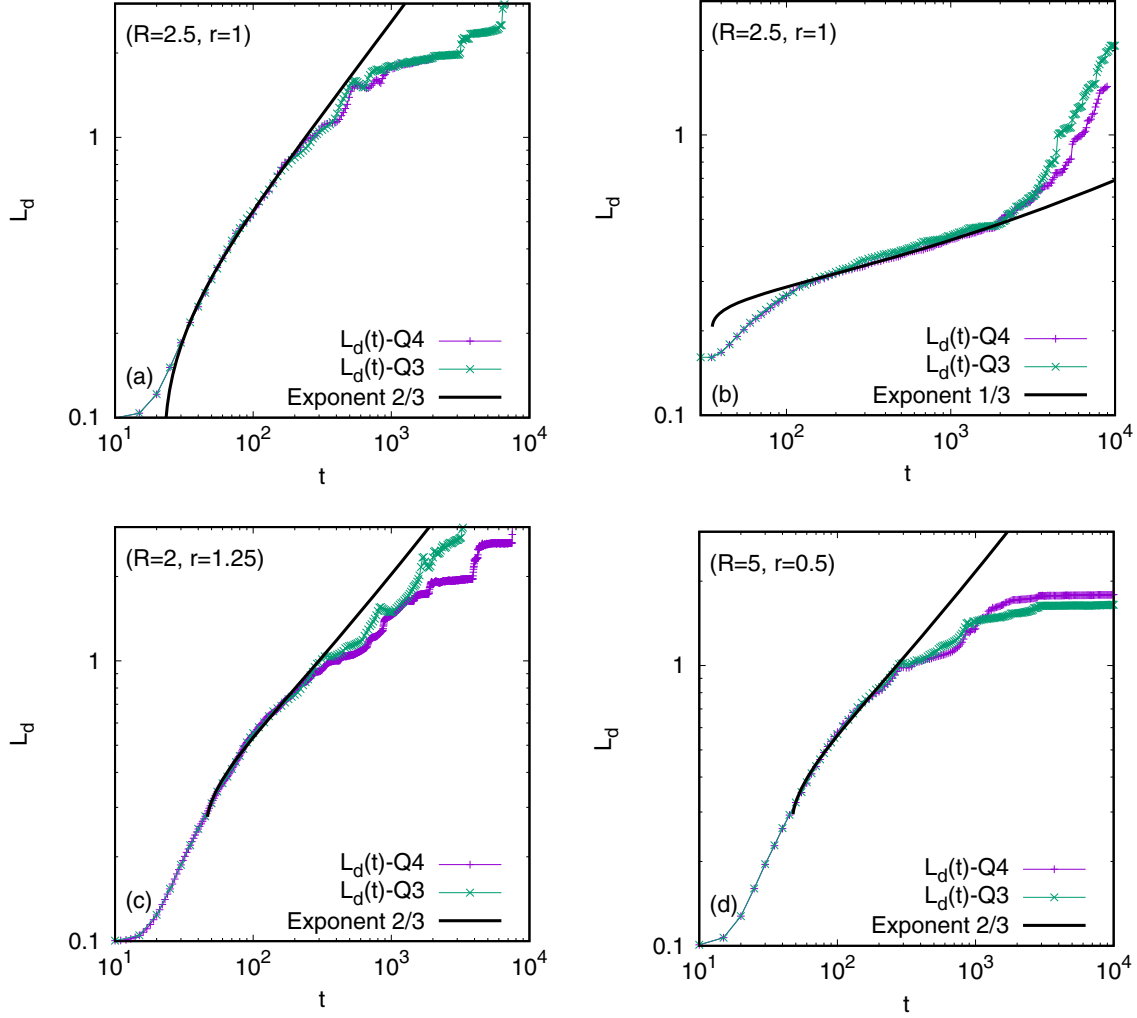
FIG. 18. Comparison of the growth of the fluid domain size $L_d(t)$ in the inertial-hydrodynamics regime on a torus for even (a), (c), (d) and uneven (b) mixtures on the tori with $R = 2.5$ and $r = 1$ (a), (b), $R = 2$ and $r = 1.25$ (c), as well as $R = 5$ and $r = 0.5$ (d). The results corresponding to $Q = 4$ and 3 are shown with purple + signs and cyan × signs, respectively. The solid line shows the best fit curve corresponding to $at^\alpha$, with $\alpha = \frac{2}{3}$ for (a), (c), (d) and $\frac{1}{3}$ for (b), to the $Q = 4$ data on the interval $30 \leqslant t \leqslant 200$ for the even mixture and $200 \leqslant t \leqslant 2000$ for the uneven mixture.

mixtures on the tori having $(R, r) = (2, 1.25)$ and $(5, 0.5)$, respectively. The $Q = 4$ results coincide with those shown in Figs. 11(a) and 11(b).

Finally, Fig. 19 shows a comparison of the domain configurations in the spinodal decomposition problem for the torus geometry. The initial fluctuations are taken around $\phi_0 = 0$ on a torus with $R = 2.5$ and $r = 1$. The $Q = 4$ snapshots, shown on the bottom line, coincide with the results shown on the middle line of Fig. 10. The agreement between the $Q = 3$ and 4 is remarkably good, with small differences observable only at the small-scale structure. Similar agreement can be seen for all decomposition cases discussed in Sec. IV.

The conclusion of this Appendix section can be summarized from the perspective of the improvements to the $Q = 3$ results brought by employing the increased quadrature order $Q = 4$. In the problem concerning the sliding drops and stripes, which is dominated by surface tension effects, the agreement is excellent and the improvement is negligible, indicating that $Q = 3$ is sufficient to capture the relevant phenomena. In the case of the domain decomposition, the early stages seem to be captured similarly with $Q = 3$ and 4. However, in the late stages of the evolution, differences can be seen, which are however irrelevant since they occur after finite size effects affect the growth dynamics. The snapshot comparison shows that the differences between the two implementations are more visible at the small-scale structure of the flow.

## APPENDIX C: FINITE DIFFERENCE SCHEMES

### 1. Cartesian geometry

In the Cartesian geometry, the Boltzmann equation reads as

$$\frac{\partial f_k}{\partial t} + v_{k_x} \frac{\partial f_k}{\partial x} + v_{k_y} \frac{\partial f_k}{\partial y} + \frac{F^x}{m}\left(\frac{\partial f}{\partial v^x}\right)_k + \frac{F^y}{m}\left(\frac{\partial f}{\partial v^y}\right)_k$$
$$= -\frac{1}{\tau}\left[f_k - f_k^{(eq)}\right], \tag{C1}$$

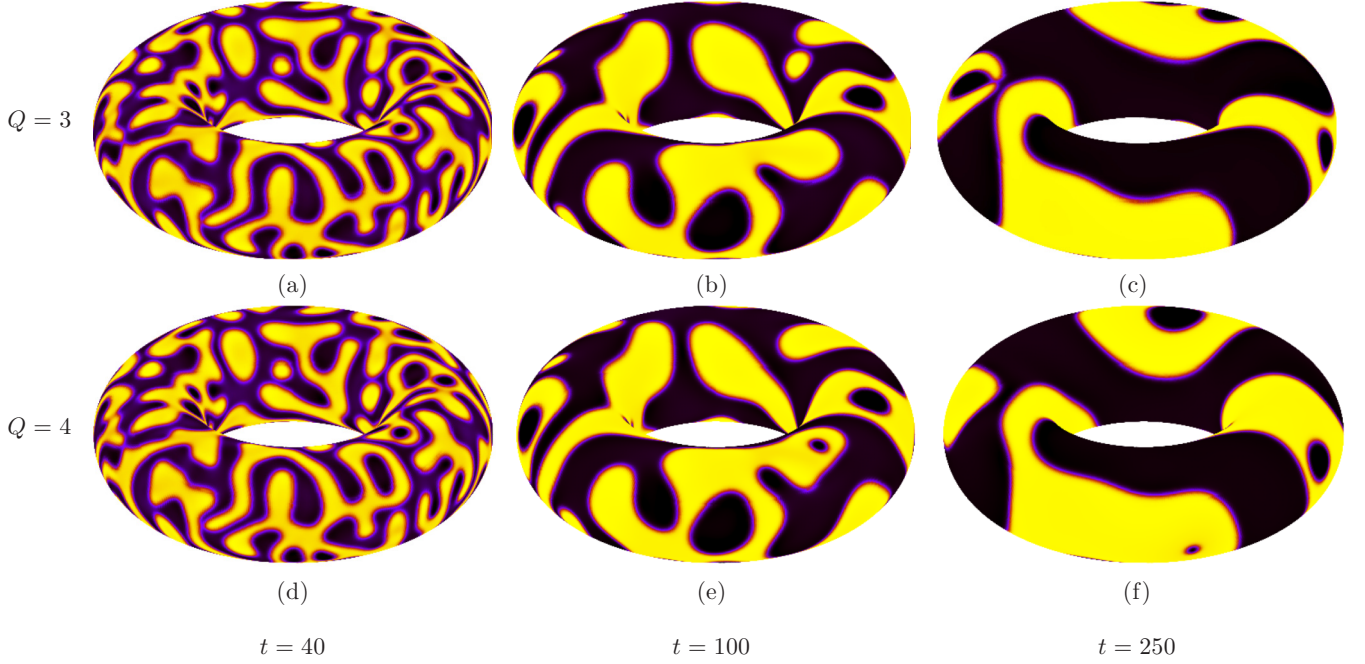where $\mathbf{k} = (k_x, k_y)$ and the components of the force term are given in Eq. (2.15).

FIG. 19. Snapshots of the typical fluid configurations at $t = 40$, 100, and 250, using the $Q = 3$ (top line) and $Q = 4$ (bottom line) implementations.

The Cahn-Hilliard equation can be written as

$$\frac{\partial \phi}{\partial t} + \frac{\partial (u^x \phi)}{\partial x} + \frac{\partial (u^y \phi)}{\partial y} = M \Delta \mu, \tag{C2}$$

where the chemical potential $\mu$ is given in Eq. (2.11).

Let $\psi(x, y)$ be a scalar function. Following the discretization of the $x$ and $y$ coordinates, $\psi(x, y)$ is replaced by a set of time-dependent quantities $\psi_{i,j}$, which are interpreted as the point values of $\psi(x, y)$ at the center $(x_i, y_j)$ of cell $(i, j)$. The gradient of $\psi(x, y)$ at $(x_i, y_j)$ is computed using the following procedure:

$$\left( \frac{\partial \psi}{\partial x} \right)_{i,j} = \frac{1}{\delta x} \left[ -\frac{1}{12} \psi_{i+2,j} + \frac{2}{3} \psi_{i+1,j} \right.$$
$$\left. -\frac{2}{3} \psi_{i-1,j} + \frac{1}{12} \psi_{i-2,j} \right],$$

$$\left( \frac{\partial \psi}{\partial y} \right)_{i,j} = \frac{1}{\delta y} \left[ -\frac{1}{12} \psi_{i,j+2} + \frac{2}{3} \psi_{i,j+1} \right.$$
$$\left. -\frac{2}{3} \psi_{i,j-1} + \frac{1}{12} \psi_{i,j-2} \right], \tag{C3}$$

where $\delta x$ and $\delta y$ are the grid spacings in the $x$ and $y$ directions, respectively. The above expressions are fourth order accurate. The Laplacian of $\psi(x, y)$ can be obtained using

$$(\Delta \psi)_{i,j} = \frac{1}{\delta x^2} \left( -\frac{1}{12} \psi_{i+2,j} + \frac{4}{3} \psi_{i+1,j} - \frac{5}{2} \psi_{i,j} \right.$$
$$\left. + \frac{4}{3} \psi_{i-1,j} - \frac{1}{12} \psi_{i-2,j} \right) + \frac{1}{\delta y^2} \left( -\frac{1}{12} \psi_{i,j+2} \right.$$
$$\left. + \frac{4}{3} \psi_{i,j+1} - \frac{5}{2} \psi_{i,j} + \frac{4}{3} \psi_{i,j-1} - \frac{1}{12} \psi_{i,j-2} \right). \tag{C4}$$

The above expression is also fourth order accurate.

The strategy in computing the force term [Eq. (2.15)] is to first obtain the set $(\Delta \phi)_{i,j}$ using the stencil in Eq. (C4), and then to apply the stencils in Eq. (C3) in order to obtain $(\partial_x \Delta \phi)_{i,j}$ and $(\partial_y \Delta \phi)_{i,j}$. Similarly, the right hand side of the Cahn-Hilliard equation [Eq. (C2)] is obtained by first computing $\mu_{i,j}$ based on the previously computed values of $(\Delta \phi)_{i,j}$, after which the Laplacian of $\mu$ is obtained by applying the stencil in Eq. (C4).

We now discuss the time evolution and advection schemes. Let us consider the evolution equation

$$\partial_t H = L[H], \tag{C5}$$

where $H$ can be either $f_k$ from Eq. (C1) or $\phi$ from Eq. (C2). The time variable is discretized using equal time steps $\delta t$, such that after $n$ time steps, the time coordinate $t_n$ has the following value:

$$t_n = n \delta t. \tag{C6}$$

Denoting $f_{k;n}$ and $\phi_n$ as the distribution function and order parameter at time step $n$, their values at time step $n + 1$ can be found via the Runge-Kutta algorithm using two intermediate steps [75]

$$H_n^{(1)} = H_n + \delta t \, L[H_n],$$
$$H_n^{(2)} = \frac{3}{4} H_n + \frac{1}{4} H_n^{(1)} + \frac{1}{4} \delta t \, L[H_n^{(1)}],$$
$$H_{n+1} = \frac{1}{3} H_n + \frac{2}{3} H_n^{(2)} + \frac{2}{3} \delta t \, L[H_n^{(2)}]. \tag{C7}$$

The advection can be computed using

$$\left( \frac{\partial (V^x H)}{\partial x} \right)_{i,j} = \frac{\mathcal{F}_{i+1/2,j}^x - \mathcal{F}_{i-1/2,j}^x}{\delta x},$$
$$\left( \frac{\partial (V^y H)}{\partial y} \right)_{i,j} = \frac{\mathcal{F}_{i,j+1/2}^y - \mathcal{F}_{i,j-1/2}^y}{\delta y}, \tag{C8}$$

where $V^x = v_{k_x}$ and $V^y = v_{k_y}$ for the Boltzmann equation [Eq. (C1)], while $V^x = u^x$ and $V^y = u^y$ for the Cahn-Hilliard equation [Eq. (C2)]. The computation of the fluxes at the cell interfaces ($\mathcal{F}_{i+1/2,j}$ and so forth) is performed in an upwind-biased manner using the fifth order weighted essentially nonoscillatory (WENO-5) algorithm introduced in [76]. This scheme is particularly well suited for flows involving strong shocks or discontinuities [77]. Other schemes such as the discontinuous Galerkin [55,78] or finite volume [79–81] may be suitable for the same purpose, however, we have not considered them in the context of this paper. For brevity, we only summarize the WENO-5 algorithm for constructing the flux for a one-dimensional problem at the interface between cells $s$ and $s+1$ for the case when the advection velocity $V_{s+1/2} = (V_{s+1} + V_s)/2$ at the cell interface is positive. When $V_{s+1/2} < 0$, the algorithm can be applied identically by symmetrically reflecting all indices with respect to $s + 1/2$, e.g., $s + 1$ becomes $s$, $s + 2$ becomes $s - 1$, etc. When $V_{s+1/2} > 0$, the flux $\mathcal{F}_{s+1/2}$ is computed using

$$\mathcal{F}_{s+1/2} = \overline{\omega}_1 \mathcal{F}_{s+1/2}^1 + \overline{\omega}_2 \mathcal{F}_{s+1/2}^2 + \overline{\omega}_3 \mathcal{F}_{s+1/2}^3, \quad \text{(C9)}$$

where the interpolating functions $\mathcal{F}_{s+1/2}^r$ ($r = 1, 2, 3$) can be written in terms of $J_s = V_s H_s$ as follows:

$$\mathcal{F}_{s+1/2}^1 = \tfrac{1}{3} J_{s-2} - \tfrac{7}{6} J_{s-1} + \tfrac{11}{6} J_s,$$
$$\mathcal{F}_{s+1/2}^2 = -\tfrac{1}{6} J_{s-1} + \tfrac{5}{6} J_s + \tfrac{1}{3} J_{s+1},$$
$$\mathcal{F}_{s+1/2}^3 = \tfrac{1}{3} J_s + \tfrac{5}{6} J_{s+1} - \tfrac{1}{6} J_{s+2}. \quad \text{(C10)}$$

The weighting factors $\overline{\omega}_r$ are defined as

$$\overline{\omega}_r = \frac{\widetilde{\omega}_r}{\widetilde{\omega}_1 + \widetilde{\omega}_2 + \widetilde{\omega}_3}, \qquad \widetilde{\omega}_r = \frac{\delta_r}{\sigma_r^2} \quad \text{(C11)}$$

with ideal weights $\delta_r$ given by

$$\delta_1 = 1/10, \quad \delta_2 = 6/10, \quad \delta_3 = 3/10, \quad \text{(C12)}$$

and the smoothness indicators $\sigma_r$ given by

$$\sigma_1 = \tfrac{13}{12}(J_{s-2} - 2J_{s-1} + J_s)^2 + \tfrac{1}{4}(J_{s-2} - 4J_{s-1} + 3J_s)^2,$$
$$\sigma_2 = \tfrac{13}{12}(J_{s-1} - 2J_s + J_{s+1})^2 + \tfrac{1}{4}(J_{s-1} - J_{s+1})^2,$$
$$\sigma_3 = \tfrac{13}{12}(J_s - 2J_{s+1} + J_{s+2})^2 + \tfrac{1}{4}(3J_s - 4J_{s+1} + J_{s+2})^2. \quad \text{(C13)}$$

The above implementation ensures third order accuracy with respect to the time step $\delta t$ and fifth order accuracy with respect to the grid spacings $\delta x$ and $\delta y$ for smooth data sets [76].

### 2. Torus geometry

After the velocity space discretization, the Boltzmann equation on the torus, given by Eq. (2.17), reads as

$$\frac{\partial f_{\boldsymbol{k}}}{\partial t} + \frac{v_{k_\theta}}{r(1 + a\cos\theta)} \frac{\partial[f_{\boldsymbol{k}}(1 + a\cos\theta)]}{\partial\theta}$$
$$+ \frac{v_{k_\varphi}}{R(1 + a\cos\theta)} \frac{\partial f_{\boldsymbol{k}}}{\partial\varphi} + \frac{F^{\hat{\theta}}}{m}\left(\frac{\partial f}{\partial v^{\hat{\theta}}}\right)_{\boldsymbol{k}} + \frac{F^{\hat{\varphi}}}{m}\left(\frac{\partial f}{\partial v^{\hat{\varphi}}}\right)_{\boldsymbol{k}}$$
$$- \frac{\sin\theta}{R(1 + a\cos\theta)}\left[v_{k_\varphi}^2\left(\frac{\partial f}{\partial v^{\hat{\theta}}}\right)_{\boldsymbol{k}} - v_{k_\theta}\left(\frac{\partial(f v^{\hat{\varphi}})}{\partial v^{\hat{\varphi}}}\right)_{\boldsymbol{k}}\right]$$
$$= -\frac{1}{\tau}[f_{\boldsymbol{k}} - f_{\boldsymbol{k}}^{(\text{eq})}], \quad \text{(C14)}$$

where $a = r/R$. The components of the force term $F^{\hat{\theta}}$ and $F^{\hat{\varphi}}$ are given through

$$nF^{\hat{\theta}} = \frac{1}{r}(\partial_\theta p_{\text{binary}} + \kappa\phi\partial_\theta\Delta\phi),$$
$$nF^{\hat{\varphi}} = \frac{1}{R(1 + a\cos\theta)}(\partial_\varphi p_{\text{binary}} + \kappa\phi\partial_\varphi\Delta\phi). \quad \text{(C15)}$$

The Cahn-Hilliard equation given in Eq. (2.12) is reproduced below explicitly for the case of the torus geometry:

$$\frac{\partial\phi}{\partial t} + \frac{1}{r(1 + a\cos\theta)} \frac{\partial[(1 + a\cos\theta)u^{\hat{\theta}}\phi]}{\partial\theta}$$
$$+ \frac{1}{R(1 + a\cos\theta)} \frac{\partial u^{\hat{\varphi}}}{\partial\varphi} = M\Delta\mu, \quad \text{(C16)}$$

where the action of the Laplace-Beltrami operator $\Delta$ on $\mu$ is

$$\Delta\mu = \frac{1}{R^2(1 + a\cos\theta)^2}\left\{\frac{\partial^2\mu}{\partial\varphi^2}\right.$$
$$\left. + \frac{1}{a^2}(1 + a\cos\theta)\frac{\partial}{\partial\theta}\left[(1 + a\cos\theta)\frac{\partial\mu}{\partial\theta}\right]\right\}. \quad \text{(C17)}$$

We now consider an equidistant discretization of the $\varphi$ and $\theta$ coordinates using $N_\varphi$ and $N_\theta$ points $\varphi_s = \frac{2\pi}{N_\varphi}(s - 1/2)$ ($1 \leqslant s \leqslant N_\varphi$) and $\theta_q = \frac{2\pi}{N_\theta}(q - 1/2)$ ($1 \leqslant q \leqslant N_\theta$). The advection terms appearing in the Boltzmann equation [Eq. (C14)] and in the Cahn-Hilliard equation [Eq. (C16)] are implemented as follows:

$$\left\{\frac{1}{R + r\cos\theta}\left[\frac{\partial(V^\theta H)}{\partial\theta} + \frac{\partial(V^\varphi H)}{\partial\varphi}\right]\right\}_{s,q} = \frac{1}{R + r\cos\theta_s}$$
$$\times \left[\frac{\mathcal{F}_{s+1/2,q}^\theta - \mathcal{F}_{s-1/2,q}^\theta}{\delta\theta} + \frac{\mathcal{F}_{s,q+1/2}^\varphi - \mathcal{F}_{s,q-1/2}^\varphi}{\delta\varphi}\right], \quad \text{(C18)}$$

where $V^\theta = \frac{R}{r}v_{k_\theta}(1 + a\cos\theta)$ and $V^\varphi = v_{k_\varphi}$ in the case of the Boltzmann equation (when $H = f_{\boldsymbol{k}}$), and $V^\theta = \frac{R}{r}u^{\hat{\theta}}(1 + a\cos\theta)$ and $V^\varphi = u^{\hat{\varphi}}$ in the case of the Cahn-Hilliard equation (when $H = \phi$). The fluxes $\mathcal{F}_{s\pm1/2,q}^\theta$ and $\mathcal{F}_{s,q\pm1/2}^\varphi$ are computed via Eq. (C9) by replacing $J_s$ with

$$J_{\boldsymbol{k};s,q}^{\theta;\text{B}} = \frac{R}{r}v_{k_\theta}(1 + a\cos\theta_q)f_{\boldsymbol{k};s,q},$$
$$J_{\boldsymbol{k};s,q}^{\varphi;\text{B}} = v_{k_\varphi}f_{\boldsymbol{k};s,q},$$
$$J_{s,q}^{\theta;\text{CH}} = \frac{R}{r}u_{s,q}^{\hat{\theta}}(1 + a\cos\theta_q)\phi_{s,q},$$
$$J_{s,q}^{\varphi;\text{CH}} = u_{s,q}^{\hat{\varphi}}\phi_{s,q}. \quad \text{(C19)}$$

This scheme retains fifth order accuracy with respect to $\delta\theta$ and $\delta\varphi$. The form of the advection operator in Eq. (C18) prompts the approximation of the connection coefficient in front of the inertial and reaction forces on line 2 in Eq. (C14) as follows:

$$\left\langle\frac{\sin\theta}{R + r\cos\theta}\right\rangle_{s,q} = \frac{\sin\theta_q}{R + r\cos\theta_q}. \quad \text{(C20)}$$

The components $F^{\hat{\theta}}$ and $F^{\hat{\varphi}}$ of the force term in Eq. (C15) are replaced by

$$F_{s,q}^{\hat{\theta}} = \frac{1}{r}\left[\frac{1}{n_{s,q}}(\partial_\theta p_{\text{binary}})_{s,q} + \frac{\kappa \phi_{s,q}}{n_{s,q}}(\partial_\theta \Delta\phi)_{s,q}\right],$$

$$F_{s,q}^{\hat{\varphi}} = \frac{1}{R + r\cos\theta_s}\left[\frac{1}{n_{s,q}}(\partial_\varphi p_{\text{binary}})_{s,q} + \frac{\kappa \phi_{s,q}}{n_{s,q}}(\partial_\varphi \Delta\phi)_{s,q}\right],$$

$$\text{(C21)}$$

where the derivatives with respect to $\theta$ and $\varphi$ are computed using the stencils given in Eq. (C3) by replacing $\psi_{s,q}$ with $(p_{\text{binary}})_{s,q}$ and $(\Delta\phi)_{s,q}$, as appropriate.

We now turn to the computation of the Laplacian. Introducing the variable

$$\chi = \frac{2a}{\sqrt{1-a^2}}\arctan\left[\sqrt{\frac{1-a}{1+a}}\tan\frac{\theta}{2}\right], \quad \text{(C22)}$$

the Laplace-Beltrami operator [Eq. (C17)] acting on the function $\psi \in \{\phi, \mu\}$ reduces to

$$\Delta\psi = \frac{1}{R^2(1 + a\cos\theta)^2}\widetilde{\Delta\psi},$$

$$\widetilde{\Delta\psi} = \frac{\partial^2\psi}{\partial\chi^2} + \frac{\partial^2\psi}{\partial\varphi^2}. \quad \text{(C23)}$$

The discrete equivalent of the above relation leads to

$$(\Delta\psi)_{s,q} = \frac{1}{(R + r\cos\theta_q)^2}(\widetilde{\Delta\psi})_{s,q}. \quad \text{(C24)}$$

The second order derivative with respect to $\varphi$ appearing in Eq. (C23) can be replaced using the stencils in Eq. (C4). The derivative with respect to $\chi$ is more difficult since the variable $\chi$ is not equidistantly discretized. The following stencil is fourth order accurate with respect to both $\delta\varphi$ and $\delta\theta$:

$$(\widetilde{\Delta\psi})_{s,q} = \frac{1}{\delta\varphi^2}\left(-\frac{1}{12}\psi_{s+2,q} + \frac{4}{3}\psi_{s+1,q} - \frac{5}{2}\psi_{s,q} + \frac{4}{3}\psi_{s-1,q} - \frac{1}{12}\psi_{s-2,q}\right)$$
$$+ a_{q;2}\psi_{s,q+2} + a_{q;1}\psi_{s,q+1} + + a_{q;0}\psi_{s,q} + a_{q;-1}\psi_{s,q-1} + a_{q;-2}\psi_{s,q-2}, \quad \text{(C25)}$$

where the coefficients $a_{q;k}$ are given below:

$$a_{q;\pm 2} = \frac{2[(\chi_q - \chi_{q\mp 1})(\chi_q - \chi_{q\mp 2}) + (\chi_q - \chi_{q\pm 1})(2\chi_q - \chi_{q\mp 1} - \chi_{q\mp 2})]}{(\chi_{q\pm 2} - \chi_{q\mp 2})(\chi_{q\pm 2} - \chi_{q+1})(\chi_{q\pm 2} - \chi_q)(\chi_{q\pm 2} - \chi_{q-1})},$$

$$a_{q;\pm 1} = \frac{2[(\chi_q - \chi_{q\mp 1})(\chi_q - \chi_{q\mp 2}) + (\chi_q - \chi_{q\pm 2})(2\chi_q - \chi_{q\mp 1} - \chi_{q\mp 2})]}{(\chi_{q\pm 1} - \chi_{q\mp 1})(\chi_{q\pm 1} - \chi_{q+2})(\chi_{q\pm 1} - \chi_q)(\chi_{q\pm 1} - \chi_{q-2})}, \quad \text{(C26)}$$

while $a_{q;0} = -a_{q;2} - a_{q;1} - a_{q;-1} - a_{q;-2}$.

[1] I. Giordanelli, M. Mendoza, and H. J. Herrmann, Sci. Rep. **8**, 12545 (2018).

[2] L. M. Schwartz and D. E. Weidner, J. Eng. Math. **29**, 91 (1995).

[3] P. D. Howell, J. Eng. Math. **45**, 283 (2003).

[4] F. C. Keber, E. Loiseau, T. Sanchez, S. J. DeCamp, L. Giomi, M. J. Bowick, M. C. Marchetti, Z. Dogic, and A. R. Bausch, Science **345**, 1135 (2014).

[5] S. Henkes, M. C. Marchetti, and R. Sknepnek, Phys. Rev. E **97**, 042605 (2018).

[6] L. M. C. Janssen, A. Kaiser, and H. Löwen, Sci. Rep. **7**, 5667 (2017).

[7] M. L. Henle and A. J. Levine, Phys. Rev. E **81**, 011905 (2010).

[8] M. Arroyo and A. Desimone, Phys. Rev. E **79**, 039906(E) (2009).

[9] J. M. Martí, R. D. Blandford, and M. J. Rees, Living Rev. Comput. Astrophys. **1**, 3 (2015).

[10] G. F. R. Ellis, R. Maartens, and M. A. H. Mac-Callum, *Relativistic Cosmology* (Cambridge University Press, Cambridge, 2012).

[11] J. M. Seddon and R. H. Templer, in *Structure and Dynamics of Membranes: From Cells to Vesicles, Handbook of Biological Physics*, Vol. 1, edited by R. Lipowsky and E. Sackmann (Elsevier, Amsterdam, 1995), Chap. 3.

[12] T. Baumgart, S. T. Hess, and W. W. Webb, Nature (London) **425**, 821 (2003).

[13] K. Bacia, P. Schwille, and T. Kurzchalia, Proc. Natl. Acad. Sci. USA **102**, 3272 (2005).

[14] A. Aufderhorst-Roberts, U. Chandra, and S. D. Connell, Biophys. J. **112**, 313 (2017).

[15] H. T. McMahon and J. L. Gallop, Nature (London) **438**, 590 (2005).

[16] R. Parthasarathy, C.-H. Yu, and J. T. Groves, Langmuir **22**, 5095 (2006).

[17] L.-L. Pontani, M. F. Haase, I. Raczkowska, and J. Brujic, Soft Matter **9**, 7150 (2013).

[18] F. Jülicher and R. Lipowsky, Phys. Rev. E **53**, 2670 (1996).

[19] J. Hu, T. Weikl, and R. Lipowsky, Soft Matter **7**, 6092 (2011).

[20] F. Paillusson, M. R. Pennington, and H. Kusumaatmaja, Phys. Rev. Lett. **117**, 058101 (2016).

[21] P. Fonda, M. Rinaldin, D. J. Kraft, and L. Giomi, Phys. Rev. E **98**, 032801 (2018).

[22] I. Nitschke, A. Voigt, and J. Wensch, J. Fluid Mech. **708**, 418 (2012).

[23] D. Marenduzzo and E. Orlandini, Soft Matter **9**, 1178 (2013).

[24] D. Jeong and J. Kim, Eur. Phys. J. E **38**, 117 (2015).

[25] P. Gera and D. Salac, R. Soc. Open Sci. **4**, 170472 (2017).

[26] R. Dimova, S. Aranda, N. Bezlyepkina, V. Nikolov, K. A. Riske, and R. Lipowsky, J. Phys.: Condens. Matter **18**, S1151 (2006).

[27] W. den Otter and S. Shkulipa, Biophys. J. **93**, 423 (2007).

[28] P. Cicuta, S. L. Keller, and S. L. Veatch, J. Phys. Chem. B **111**, 3328 (2007).

[29] B. A. Camley and F. L. Bown, J. Chem. Phys. **135**, 225106 (2011).

[30] T. Krüger, H. Kusumaatmaja, A. Kuzmin, O. Shardt, G. Silva, and E. M. Viggen, *Lattice Boltzmann Method: Principles and Practice* (Springer, Basel, 2017).

[31] S. Succi, *The Lattice Boltzmann Equation: For Fluid Dynamics and Beyond* (Oxford University Press, Oxford, 2001).

[32] H. Liu, Q. Kang, C. R. Leonardi, S. Schmieschek, A. Narváez, B. D. Jones, J. R. Williams, A. J. Valocchi, and J. Harting, Comput. Geosci. **20**, 777 (2016).

[33] M. S. Sadullah, C. Semprebon, and H. Kusumaatmaja, Langmuir **34**, 8112 (2018).

[34] S. Varagnolo, D. Ferraro, P. Fantinel, M. Pierno, G. Mistura, G. Amati, L. Biferale, and M. Sbragaglia, Phys. Rev. Lett. **111**, 066101 (2013).

[35] Y. Liu, M. Andrew, J. Li, J. M. Yeomans, and Z. Wang, Nat. Commun. **6**, 10034 (2015).

[36] M. R. Swift, E. Orlandini, W. R. Osborn, and J. M. Yeomans, Phys. Rev. E **54**, 5041 (1996).

[37] X. Shan and H. Chen, Phys. Rev. E **47**, 1815 (1993).

[38] A. K. Gunstensen, D. H. Rothman, S. Zaleski, and G. Zanetti, Phys. Rev. A **43**, 4320 (1991).

[39] C. Semprebon, T. Krüger, and H. Kusumaatmaja, Phys. Rev. E **93**, 033305 (2016).

[40] M. Wöhrwag, C. Semprebon, A. Mazloomi Moqaddam, I. Karlin, and H. Kusumaatmaja, Phys. Rev. Lett. **120**, 234501 (2018).

[41] R. H. H. Abadi, A. Fakhari, and M. H. Rahimian, Phys. Rev. E **97**, 033312 (2018).

[42] H. Liang, B. C. Shi, and Z. H. Chai, Phys. Rev. E **93**, 013308 (2016).

[43] K. S. Ridl and A. J. Wagner, Phys. Rev. E **98**, 043305 (2018).

[44] T. J. Spencer and C. M. Care, Phys. Rev. E **74**, 061708 (2006).

[45] C. Denniston, E. Orlandini, and J. M. Yeomans, Phys. Rev. E **63**, 056702 (2001).

[46] O. Malaspinas, N. Fiétier, and M. Deville, J. Nonnewton. Fluid Mech. **165**, 1637 (2010).

[47] A. Gupta, M. Sbragaglia, and A. Scagliarini, J. Comput. Phys. **291**, 177 (2015).

[48] M. Mendoza, S. Succi, and H. J. Herrmann, Sci. Rep. **3**, 3106 (2013).

[49] L. Budinsky, Comput. Fluids **96**, 288 (2014).

[50] J.-D. Debus, M. Mendoza, S. Succi, and H. J. Herrmann, Sci. Rep. **7**, 42350 (2017).

[51] A. M. Velasco, J. D. M. Noz, and M. Mendoza, J. Comput. Phys. **376**, 76 (2019).

[52] Z. Guo and T. S. Zhao, Phys. Rev. E **67**, 066709 (2003).

[53] M. Watari, J. Fluids Eng. **138**, 011202 (2016).

[54] K. Hejranfar, M. H. Saadat, and S. Taheri, Phys. Rev. E **95**, 023314 (2017).

[55] K. Hejranfar and M. Hajihassanpour, Comput. Fluids **156**, 175 (2017).

[56] L. Mieussens, J. Comput. Phys. **162**, 429 (2000).

[57] M. T. Ho and I. Graur, Int. J. Heat Mass Transfer **90**, 58 (2015).

[58] S. Busuioc and V. E. Ambruş, Phys. Rev. E **99**, 033304 (2019).

[59] C. Y. Cardall, E. Endeve, and A. Mezzacappa, Phys. Rev. D **88**, 023011 (2013).

[60] S. Busuioc, H. Kusumaatmaja, and V. E. Ambruş, arXiv:1911.06401 [physics.flu-dyn].

[61] A. J. Bray, Adv. Phys. **51**, 481 (2002).

[62] V. M. Kendon, M. E. Cates, I. Pagonabarraga, J. C. Desplat, and P. Bladon, J. Fluid Mech. **440**, 147 (2001).

[63] A. J. Wagner and J. M. Yeomans, Phys. Rev. Lett. **80**, 1429 (1998).

[64] A. J. Briant and J. M. Yeomans, Phys. Rev. E **69**, 031603 (2004).

[65] M. Rieutord, *Fluid Dynamics: An Introduction* (Springer, Cham, 2015).

[66] Q. Li and A. J. Wagner, Phys. Rev. E **76**, 036701 (2007).

[67] C. Cercignani, *The Boltzmann Equation and its Applications* (Springer, New York, 1988).

[68] P. J. Dellar, Phys. Rev. E **64**, 031203 (2001).

[69] A. J. Wagner and M. E. Cates, Europhys. Lett. **56**, 556 (2001).

[70] V. Sofonea, T. Biciuşcă, S. Busuioc, V. E. Ambruş, G. Gonnella, and A. Lamura, Phys. Rev. E **97**, 023309 (2018).

[71] V. E. Ambruş and V. Sofonea, J. Comput. Phys. **316**, 1 (2016).

[72] X. Shan, X.-F. Yuan, and H. Chen, J. Fluid Mech. **550**, 413 (2006).

[73] S. Busuioc, V. E. Ambruş, T. Biciuşcă, and V. Sofonea, Comput. Math. Appli. (to be published, 2019), doi:10.1016/j.camwa.2018.12.015.

[74] V. E. Ambruş and V. Sofonea, in *Flowing Matter*, edited by F. Toschi and M. Sega (Springer, Cham, 2019), Chap. 9, pp. 271–299.

[75] C.-W. Shu and S. Osher, J. Comput. Phys. **77**, 439 (1988).

[76] G. S. Jiang and C. W. Shu, J. Comput. Phys. **126**, 202 (1996).

[77] Y. Gan, A. Xu, G. Zhang, and Y. Li, Phys. Rev. E **83**, 056704 (2011).

[78] T. Lee and C.-L. Lin, J. Comput. Phys. **171**, 336 (2001).

[79] F. Nannelli and S. Succi, J. Stat. Phys. **68**, 401 (1992).

[80] D. Patil and K. N. Lakshmisha, J. Comput. Phys. **228**, 5262 (2009).

[81] W. Li and L.-S. Luo, Commun. Comput. Phys. **20**, 301 (2016).